



<b>Publication Year</b>	2017
<b>Acceptance in OA</b>	2020-09-04T10:51:30Z
<b>Title</b>	Global permittivity mapping of the Martian surface from SHARAD
<b>Authors</b>	Castaldo, Luigi, Mège, Daniel, Gurgurewicz, Joanna, OROSEI, ROBERTO, Alberti, Giovanni
<b>Publisher's version (DOI)</b>	10.1016/j.epsl.2017.01.012
<b>Handle</b>	<a href="http://hdl.handle.net/20.500.12386/27137">http://hdl.handle.net/20.500.12386/27137</a>
<b>Journal</b>	EARTH AND PLANETARY SCIENCE LETTERS
<b>Volume</b>	462

Elsevier Editorial System(tm) for Earth and  
Planetary Science Letters

Manuscript Draft

Manuscript Number: EPSL-D-16-00299

Title: Global permittivity mapping of the Martian surface from SHARAD

Article Type: Letters

Keywords: subsurface sounder; Mars; ice; dichotomy boundary; permittivity constant; dielectric properties

Corresponding Author: Dr. Luigi Castaldo, Ph.D.

Corresponding Author's Institution: Polish Academy of Sciences

First Author: Luigi Castaldo, Ph.D.

Order of Authors: Luigi Castaldo, Ph.D.; Daniel Mège; Joanna Gurgurewicz; Roberto Orosei; Giovanni Alberti

Abstract: SHARAD is a subsurface sounding radar aboard NASA's Mars Reconnaissance Orbiter, capable of detecting dielectric discontinuities in the subsurface caused by compositional and/or structural changes. Echoes coming from the surface contain information on geometric properties at meter scale and on the dielectric permittivity of the upper layers of the Martian crust. A model has been developed to estimate the effect of surface roughness on echo power, depending on statistical parameters such as RMS height and topography. Such model is based on the assumption that topography can be characterized as a self-affine fractal, and its use allows the estimation of the dielectric properties of the first few meters of the Martian soil. A permittivity map of the surface of Mars is obtained, covering several large regions across the planet surface. The most significant correspondence with geology is observed at the dichotomy boundary, with high dielectric constant on the highlands side (7 to over 10) and lower on the lowlands side (3 to 7). Other geological correlations are discussed.

Suggested Reviewers: Cyril Grima  
cgrima@ig.utexas.edu

Bruce A. Campbell  
campbellb@si.edu

Jeremie Mougino  
jmougino@uci.edu

Thomas Watters  
watterst@si.edu

Yonggyu Gim  
yonggyu.gim@jpl.nasa.gov

Opposed Reviewers:





CENTRUM BADAŃ KOSMICZNYCH PAN – SPACE RESEARCH CENTRE PAS

UL. BARTYCKA 18A • 00-716 WARSZAWA • POLAND

Daniel MÈGE, Visiting Professor, e-mail: daniel.mege@cbk.waw.pl, phone: +48 50 600 59 62

---

Wrocław, March 10<sup>th</sup>, 2016

Dear EPSL Editor,

The manuscript "Global permittivity mapping of the Martian surface from SHARAD", by L. Castaldo, D. Mège, J. Gurgurewicz, R. Orosei, and G. Alberti presents the first global mapping of the permittivity constant of the Martian surface using SHARAD orbital ground-penetrating radar data, and the first global mapping of the topography of the Martian surface using MOLA products.

Previous mapping, using a different approach, was done from MARSIS data by Mouginot et al. (2010, Icarus 210, 612-625). They portray a different view of the planet's shallow subsurface due to the wavelength difference between MARSIS and SHARAD. The SHARAD maximum penetration depth is ca. 15 m, whereas the MARSIS maximum penetration depth is ten times more. An illustration of the difference in sampled crustal thickness is that the geometry of the Martian dichotomy in the subsurface is much more accurately followed with SHARAD than with MARSIS. Other examples of permittivity constant correlation with geology are discussed.

The results presented in this manuscript are of interest to researchers working on the properties of the Martian surface and subsurface, including the permafrost, its thickness and distribution. This community includes researchers working on climatic and hydrologic evolution of Mars, as well as geomorphologists and glaciologists.

Thank you for considering the opportunity of reviewing it in EPSL.

Best regards,

Daniel Mège, on behalf of the manuscript's authors

## \*Highlights (for review)

- SHARAD is capable of detecting dielectric discontinuities in the subsurface
- A permittivity map of the surface of Mars from SHARAD data is presented
- Correspondence with geology is discussed

1 **Global permittivity mapping of the Martian surface from SHARAD**

2

3 Luigi Castaldo<sup>a\*</sup>, Daniel Mège<sup>b,c,d</sup>, Joanna Gurgurewicz<sup>a,b</sup>, Roberto Orosei<sup>c</sup>, Giovanni Alberti<sup>f</sup>

4

5 <sup>a</sup>Institute of Geological Sciences, Polish Academy of Sciences, Research Centre in Wrocław, Podwale St. 75,  
6 50-449 Wrocław, Poland

7 <sup>b</sup>Space Research Centre, Polish Academy of Sciences, Bartycka St. 18A, 00-716 Warsaw, Poland

8 <sup>c</sup>Laboratoire de Planétologie et Géodynamique, CNRS UMR 6112, Université de Nantes, BP 92208, 44322  
9 Nantes cedex 3, France

10 <sup>d</sup>Observatoire des Sciences del' Univers Nantes Atlantique (OSUNA, CNRS UMS 3281), France

11 <sup>e</sup>Istituto di Radioastronomia, Istituto Nazionale di Astrofisica, Via Piero Gobetti 101, I-40129 Bologna, Italy

12 <sup>f</sup>Consorzio di Ricerca sui Sistemi di Telesensori Avanzati (CO.RI.S.T.A.), Via J. F. Kennedy 5, 80125  
13 Napoli, Italy

14

15 Luigi Castaldo: [luigi.castaldo@gmail.com](mailto:luigi.castaldo@gmail.com); Daniel Mège: [daniel.mege@univ-nantes.fr](mailto:daniel.mege@univ-nantes.fr); Joanna Gurgurewicz:  
16 [jgur@cbk.waw.pl](mailto:jgur@cbk.waw.pl); Roberto Orosei: [roberto.oroisei@inaf.it](mailto:roberto.oroisei@inaf.it); Giovanni Alberti: [giovanni.alberti@corista.eu](mailto:giovanni.alberti@corista.eu)

17

18 **Abstract**

19 SHARAD is a subsurface sounding radar aboard NASA's Mars Reconnaissance Orbiter, capable of detecting  
20 dielectric discontinuities in the subsurface caused by compositional and/or structural changes. Echoes  
21 coming from the surface contain information on geometric properties at meter scale and on the dielectric  
22 permittivity of the upper layers of the Martian crust. A model has been developed to estimate the effect of  
23 surface roughness on echo power, depending on statistical parameters such as RMS height and topography.  
24 Such model is based on the assumption that topography can be characterized as a self-affine fractal, and its  
25 use allows the estimation of the dielectric properties of the first few meters of the Martian soil. A permittivity  
26 map of the surface of Mars is obtained, covering several large regions across the planet surface. The most  
27 significant correspondence with geology is observed at the dichotomy boundary, with high dielectric  
28 constant on the highlands side (7 to over 10) and lower on the lowlands side (3 to 7). Other geological  
29 correlations are discussed.

30

31 **Keywords:** subsurface sounder, Mars, ice, dichotomy boundary, permittivity constant, dielectric properties

32

### 33 **1. Introduction**

34 Ground Penetrating Radar (GPR) is a well-established geophysical technique employed for more than five  
35 decades to investigate the terrestrial subsurface. It is based on the transmission of radar pulses at frequencies  
36 in the MF, HF and VHF portions of the electromagnetic spectrum into the surface, to detect reflected signals  
37 from subsurface structures (see e.g. Bogorodsky et al. 1985). Orbiting GPR have been successfully employed  
38 in planetary exploration (Phillips et al. 1973, Picardi et al. 2004, Seu et al. 2007, Ono et al. 2009), and are  
39 often called subsurface radar sounders. By detecting dielectric discontinuities associated with compositional  
40 and/or structural discontinuities, radar sounders are the only remote sensing instruments allowing the study  
41 of the subsurface of a planet from orbit.

42 SHARAD (Shallow Radar) is a synthetic-aperture, orbital sounding radar carried by NASA's Mars  
43 Reconnaissance Orbiter (Seu et al. 2007). SHARAD is capable of a vertical resolution of 15 m or less  
44 (depending on the dielectric permittivity of the material being sounded), operating at a central frequency of  
45 20 MHz and transmitting a 10 MHz bandwidth. SHARAD data consist of radar echoes acquired  
46 continuously along the ground track of the spacecraft during an interval of time. Although data are used  
47 mostly to study subsurface structures, surface reflections contain information on the first few meters of the  
48 Martian soil (Grima et al. 2012, Campbell et al. 2013). This paper presents a method to extract such  
49 information through the inversion of the surface echo waveform. Most backscattering models separate the  
50 effect of the permittivity constant from the remaining parameters (Currie 1984) – radar viewing geometry,  
51 scattering from a random rough surface, and volume scattering – that have thus been modelled separately to  
52 estimate their contribution to echo power. Once the correction for these contribution is applied, a surface  
53 map of dielectric permittivity can be produced for those areas on Mars for which a sufficiently dense  
54 coverage is available.

55 The MOLA laser altimeter data grid (Smith et al. 2001) is the only global topographic dataset currently  
56 available for Mars, but its horizontal resolution is too coarse to allow a precise simulation of surface  
57 scattering at SHARAD wavelengths. For this reason, a statistical model based on the theory of  
58 electromagnetic scattering from fractal surfaces (Franceschetti et al. 2007) was used to estimate the effects of

59 surface roughness and slope on scattering, and the MOLA dataset was used to compute statistical geometric  
60 parameters such as RMS height and RMS slope (Kreslavsky and Head 1999). An additional factor affecting  
61 inversion is the lack of an absolute calibration for SHARAD data, as antenna gain could not be characterized  
62 on ground due to the large size and long operational wavelength. The present work made use of more than 2  
63 TB of publicly available data acquired by SHARAD between 2006 and 2013, requiring the use of high-  
64 performance computers for processing, and the development of specialized algorithms to filter data and  
65 extract surface echo waveforms.

66 In the following sections data and methods are described, then a global permittivity map of Mars from  
67 SHARAD is presented and discussed. Comparison with information from other datasets illustrates how  
68 SHARAD reflectivity correlates with geology in several sites of geologic importance.

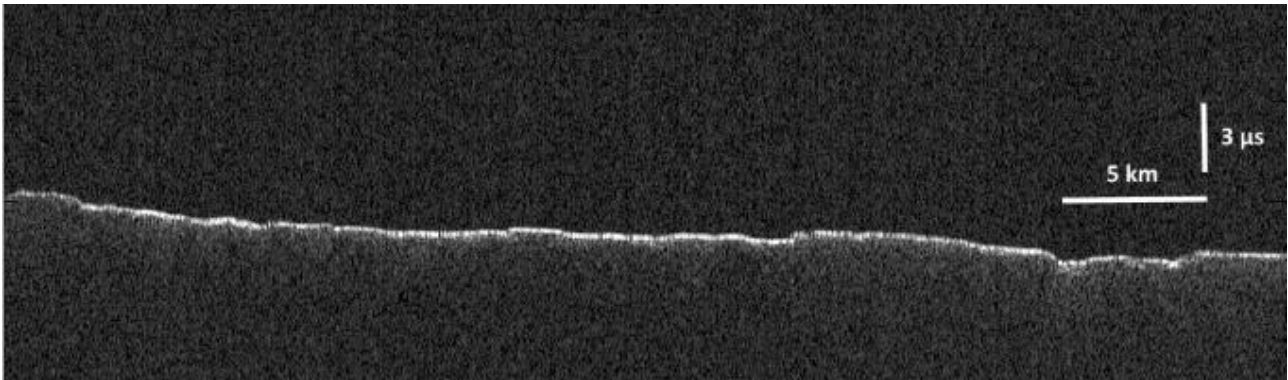
69

## 70 **2. SHARAD data**

71 The SHARAD data used in this study have been retrieved from the public archive at NASA's Planetary Data  
72 System Geosciences Node (<http://pds-geosciences.wustl.edu/missions/mro/sharad.htm>). SHARAD achieves  
73 its spatial resolution, both in depth and along the ground track, only after processing of the received echo on  
74 ground. The vertical resolution is achieved through range processing, and horizontal resolution is enhanced  
75 through synthetic aperture processing. The final data after ground processing are the SHARAD Reduced  
76 Data Records (RDR), consisting of radar echoes that have been Doppler filtered, range compressed and  
77 converted to complex voltages, complemented by proper engineering and spacecraft information (Slavney  
78 and Orosei 2008). Although, as mentioned earlier, absolute calibration of SHARAD data is not possible, the  
79 electronics of the SHARAD instrument have been fully characterized by on-ground testing and a  
80 compensation of effects other than antenna gain has been applied. SHARAD antenna pattern deviates from  
81 that of a simple dipole due to the presence of large spacecraft appendages such as the high-gain antenna and  
82 solar panels (Seu et al. 2007), but gain variations due to roll of the satellite have been corrected in order to  
83 obtain a relative calibration of the data with a precision of  $\sim 1.5$  dB (Slavney and Orosei 2008).

84 Data processing performed on board is very limited in order to simplify instrument operations, and consists  
85 mainly in coherent summing of the received echoes. SHARAD can be programmed to sum a variable  
86 number of echoes and to compress data to a different number of bits per sample. Different settings of the

87 instrument are called operational modes. The signal gain compensation due to different operational modes  
88 has to be determined on ground and applied to the data. SHARAD data are usually displayed in the form of a  
89 radargram, that is a representation of radar echoes acquired continuously during the movement of the  
90 spacecraft as a grey-scale image, in which the horizontal dimension is distance along the ground track, the  
91 vertical dimension is the round trip time of the echo, and the brightness of the pixel is a function of the  
92 strength of the echo. An example of radargram is shown in Figure 1.



93  
94 **Figure 1. Observation 0659501 001 SS19 700A is an example of a SHARAD radargram showing**  
95 **reflections due to dielectric interfaces at the surface and in the subsurface from which is extracted the**  
96 **surface power echo in linear scale by the automatic routine and low-pass filtered and weighted with**  
97 **linear least squares with a second degree polynomial model.**

98  
99 Plasma in the Martian ionosphere acts as a dispersive medium, and causes the SHARAD pulse to broaden,  
100 reducing resolution and peak power. Because the ionosphere is excited by solar radiation, dispersion  
101 decreases as the solar zenith angle (SZA) increases, becoming minimal during the night. In order to avoid  
102 filtering and compensation due to the ionosphere distortion, only data acquired on the night side of Mars  
103 have been used.

104 In the postprocessing to extract the surface echo waveform, the SHARAD signal is oversampled in range to  
105 better locate the maximum power value, assumed to be located within the surface echo. A low-pass filtering  
106 operating in azimuth and adopting a local regression using weighted linear least squares and a 2nd degree  
107 polynomial model on the radargrams is used in order to improve the signal-to-noise ratio. This avoids  
108 fluctuation of the signal power due to the horizontal resolution along track which depends on ground  
109 processing and thus is not the same for all RDR's, ranging between 0.3 km and 1 km (Seu et al. 2007). Noise  
110 is estimated from the data in which backscattering is not expected. Surface echo detection is validated by  
111 comparing its time of arrival with that computed using the spacecraft position and MOLA data.

112 The scattering model used to estimate the effect of surface roughness on echo strength is based on the  
 113 assumption that the Martian topography can be described as a self-affine fractal as in Orosei et al. (2003),  
 114 allowing the extrapolation of its statistical properties at scales smaller than MOLA resolution. Franceschetti  
 115 et al. (1999) developed a model for the backscattering coefficient of a self-affine natural surface using the  
 116 fractional Brownian motion under the Kirchhoff approximation. The topothesy is one of the statistical  
 117 parameters needed by the Franceschetti et al. (1999) model, and is estimated through the Allan variance in  
 118 the bi-dimensional space. The approach used for the estimation is described in Franceschetti et al. (2007).  
 119 The RMS deviation of a point on the surface as a function of step size is calculated with the following  
 120 formula:

$$121 \quad v(\Delta s\_lon, \Delta s\_lat) = \sqrt{\frac{1}{m} \frac{1}{n} \sum_{i=1}^m \sum_{i=1}^n [z(x_i, y_i) - z(x_i + \Delta s\_lon, y_i + \Delta s\_lat)]^2} \quad (1)$$

122 where  $m$  and  $n$  are the number of samples in the  $x$  and  $y$  directions,  $z$  is the elevation, and  $\Delta x$  and  $\Delta y$  the step  
 123 size in the  $x$  and  $y$  directions.

124 To evaluate the incidence angle of the radar pulse, the unit vector normal to the surface is then computed.  
 125 Slope is evaluated as the gradient of the topographic data within a given area and the  $x$ ,  $y$  and  $z$  components  
 126 of the local normal are then computed as follows:

$$127 \quad cx = \frac{-slope\_lon}{\sqrt{1 + slope\_lon^2} \sqrt{1 + slope\_lat^2}}$$

$$128 \quad cy = \frac{-slope\_lat}{\sqrt{1 + slope\_lon^2} \sqrt{1 + slope\_lat^2}}$$

$$129 \quad cz = \frac{1}{\sqrt{1 + slope\_lon^2} \sqrt{1 + slope\_lat^2}} \quad (2)$$

130 The incidence angle is then evaluated as:

$$131 \quad \mathcal{G} = \arccos(Rx \cdot cx + Ry \cdot cy + Rz \cdot cz) \quad (3)$$

132 where  $R_x$ ,  $R_y$  and  $R_z$  are the components of the position vector from the surface to the spacecraft.

133 The antenna pattern is introduced to take into account the azimuth resolution of the radar and the off-nadir  
 134 contribution to the scattering. The azimuth pattern is related to the theoretical azimuth resolution of 300 m as  
 135 follows (Ulaby et al. 1986):

136 
$$G_{AZ}(\vartheta_{AZ}) = \left[ \sin c \left( \frac{\vartheta_{AZ} - 0.88}{\vartheta_{3dBAZ}} \right) \right]^2$$
 (4)

137 where

138 
$$\vartheta_{3dBAZ} = 2 \cdot \text{atan} \left( \frac{\rho_{az}}{2 \cdot H_{SAT}} \right)$$

139 and  $\rho_{az}$  is the azimuth resolution.

### 140 3. SHARAD signal power evaluation

141 For a nadir-looking synthetic aperture sounder, the signal to noise ratio (SNR) can be computed as the ratio  
 142 between the signal power backscattered from Mars surface ( $P_s$ ) and the system thermal noise power ( $P_N$ )  
 143 (Seu et al. 2004):

144 
$$SNR = \frac{P_s}{P_N} = \frac{P_t G^2 \lambda^2 \sigma^0 A}{(4\pi)^3 H_s^4 L P_N} \tau B_t N$$
 (5)

145 where  $P_t$  is the transmitted peak power,  $G$  the antenna gain,  $\lambda$  the wavelength,  $\sigma^0$  the surface  
 146 backscattering coefficient,  $A$  the area of the ground resolution cell,  $\tau$  the transmitted pulse width,  $N$  the  
 147 number of coherently integrated pulses within the synthetic aperture,  $H_s$  the spacecraft altitude,  $L$  the  
 148 propagation losses, and:

149 
$$P_N = K T_s B_t$$
 (6)

150 
$$A \cdot N = \frac{\lambda \cdot H_s \cdot \text{PRF}}{V_t} \sqrt{\frac{H_s c}{B_t}}$$
 (7)

151 where  $B_t$  is the transmitted bandwidth,  $K$  the Boltzmann constant,  $T_s$  the system temperature,  $c$  the light  
 152 speed, PRF the pulse repetition frequency, and  $V_t$  the spacecraft tangential velocity.

153 The above expressions allow to evaluate the signal power ( $P_I$ ) directly, as the squared value of the generic  
 154 pixel on the range and azimuth processed SHARAD radargram:

155 
$$P_I = S_s \cdot G_{REC} \cdot C_{ADC} \cdot C_{PROC}$$
 (8)

156 where  $G_{REC}$  is the instrument receiving gain,  $C_{ADC}$  and  $C_{PROC}$  are the power conversion factors of signal  
 157 digitization and Level-1b processing. Equation (8) can be rearranged in order to isolate the terms depending  
 158 on imaged area  $\sigma^0$ , instrument operational mode (PRF) and orbit ( $H_S$  and  $V_t$ ), i.e.:

$$159 \quad P_I = C_I \frac{\sqrt{H_S}}{H_S^3 V_t} \cdot PRF \cdot \sigma^0 \quad (9)$$

160 where  $C_I$  is a constant term (independent on Mars surface and instrument operational mode and orbit),  
 161 given by:

$$162 \quad C_I = G_{REC} C_{ADC} C_{PROC} \frac{P_t G^2 \lambda^3 \tau B_t}{(4\pi)^3 L} \sqrt{\frac{c}{B_t}} \quad (10)$$

163 The use of Equations (5)-(10) to estimate the absolute power of the radar echo requires the assumptions that  
 164 (1) the antenna gain is supposed to be constant because the effects of spacecraft attitude and terrain slope are  
 165 considered negligible with respect to the large 3 dB antenna aperture; (2) the backscattering coefficient is a  
 166 function of the angle ( $\theta$ ) between the generic pixel-to-instrument line of sight and the local surface normal,  
 167 i.e.  $\sigma^{0(\theta)}$ , and that can be approximated with the local slope. It also depends on dielectric and topographic  
 168 properties of surface, which are detailed in the next paragraph.

169

#### 170 **4. Surface backscattering modelling**

171 The backscattering coefficient of the Martian surface can be modeled as proposed by Alberti et al. (2012),  
 172 i.e. by using a fractal characterization. This formulation has been used in the description of natural surfaces  
 173 because it can properly account for the scale invariance property typical of such surfaces.

174 Mandelbrot (1983) shows that statistical parameters usually employed to describe natural surfaces (i.e.,  
 175 standard deviation and correlation length) change when the observation scale changes. Conversely, the  
 176 fractal parameters of a natural surface are independent of the observation scale. The most useful fractal  
 177 model for natural surfaces is the fractional Brownian motion (fBm) (Franceschetti et al., 1999), which carries  
 178 the advantage of performing analytical evaluation of electromagnetic scattering. The mean-square value of  
 179 the field scattered along an arbitrary direction by a surface illuminated by a plane wave can be evaluated in a

180 closed form, with the Physical Optics (PO) solution under the Kirchhoff Approximation (KA) (Franceschetti  
 181 et al., 1999). Therefore the backscattering coefficient can be written as:

$$182 \quad \sigma^0(\theta) = 2k^2 \cdot \cos^2 \theta \cdot R_s^2(\theta) \cdot \int_0^\infty J_0(2k\delta \sin \theta) \cdot \exp(-2k^2 s^2 \delta^{2H} \cos^2 \theta) \delta d\delta \quad (11)$$

183 where  $\delta$  is the generic distance between two points on the surface,  $J_0$  is the zero-order Bessel function of first  
 184 kind,  $k = 2\pi/\lambda$  is the wavenumber and  $R(\theta)^2$  is the surface power Fresnel coefficient (the reflectivity),  
 185 given by:

$$186 \quad R_s^2(\theta) = \left[ \frac{\cos \theta - \sqrt{\epsilon_s - \sin^2 \theta}}{\cos \theta + \sqrt{\epsilon_s - \sin^2 \theta}} \right]^2 \quad (12)$$

187 where  $\epsilon_s$  is the real part of the surface dielectric relative constant.

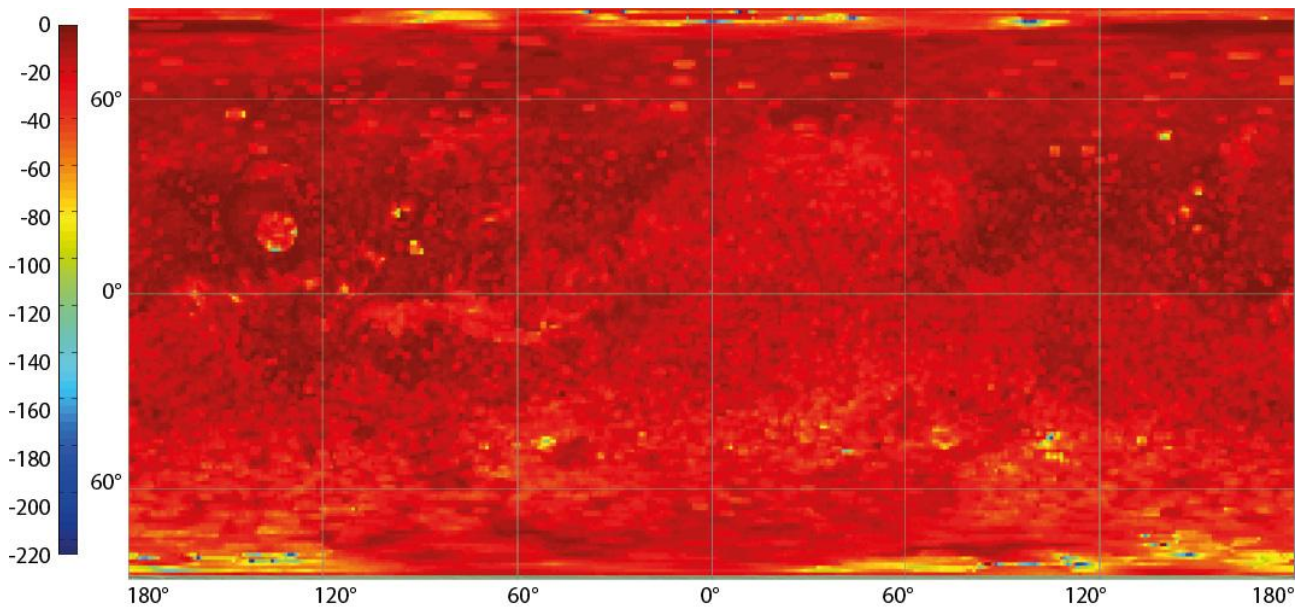
188 The previous expression involves the definition of two characteristic fractal parameters:

189  $H$ , the Hurst coefficient ( $0 < H < 1$ ), related to the fractal dimension  $D$  through the relationship  $D = 3 - H$ , and  $s$ ,  
 190 the standard deviation of surface increments at unitary distance, a real parameter related to an  $fBm$   
 191 characteristic length, the topothesy  $T$ , by means of the relationship:

$$192 \quad s = T^{(1-H)} \quad (13)$$

193 Both the Hurst coefficient and topothesy have been evaluated over the whole Mars surface using the MOLA  
 194 topographic dataset. Topothesy map is shown in Figure 2.

195



196

197 **Figure 2. Mars topothesy evaluated using MOLA topographic data**

198

199 The surface backscattering coefficient can be rewritten by isolating the factor that accounts for geometric  
200 effects due to the fractal characteristics of surface:

$$201 \quad \sigma^0(\theta) = R_s^2(\epsilon_s, \theta) \cdot \chi(H, T, \theta) \quad (14)$$

202 At nadir, the expression of backscattering coefficient can be significantly simplified (Ivanov et al. 2006):

$$203 \quad \sigma^0(0) = \frac{k^2 |R(0)|^2 T^2}{H} \frac{\Gamma\left(\frac{1}{H}\right)}{(\sqrt{2kT})^{2/H}} \quad (15)$$

204 where  $\Gamma$  is the Gamma function.

205

## 206 **5. Absolute calibration**

207 Absolute calibration of SHARAD radargrams can be achieved by compensating all effects due to both  
208 instrument and surface characteristics, such as local slope and roughness, in order to estimate the actual  
209 permittivity of the Martian surface. To this aim, it is necessary to establish as a reference the power  
210 backscattered by a Martian region with known surface physical characteristics, composition and permittivity.  
211 The selected region should be homogeneous and smooth at the scales of the SHARAD wavelength as much  
212 as possible in order to make the diffuse component of backscattered power negligible. The selected  
213 calibration area is located between 82 and 84°N, and 180 and 200°E. The area consists primarily of water ice  
214 and the value of the real part of the permittivity constant is 3.14 (Grima et al., 2009). Determining an  
215 absolute calibration constant using the reference area involves the following steps:

- 216 - detection of surface echo and evaluation of its power  $P_{Iref}$  over the reference area;
- 217 - evaluation of fractal parameters ( $H_{ref}$  and  $T_{ref}$ ) over the reference area using MOLA topographic  
218 data;
- 219 - evaluation of the reference backscattering coefficient ( $\sigma_{ref}^0$ ) through Equation (15) using the  
220 previously computed values of reference permittivity and fractal parameters;
- 221 - evaluation of the calibration constant  $C_I$  by inverting Equation (10) and averaging over all reference  
222 pixels:

$$C_I = \left\langle P_{Iref} \frac{H_{Sref}^3 V_{tref}}{\sqrt{H_{Sref} \cdot PRF_{ref} \cdot \sigma_{ref}^0}} \right\rangle \quad (16)$$

The value of surface power  $P_I$  is determined for each echo to be calibrated, together with the evaluation of fractal parameters ( $H$  and  $T$ ) and local slope ( $\theta$ ) using MOLA topographic data.

The backscattering coefficient is then estimated inverting Equation (10), using also the ancillary data within the RDR ( $H_s, V_t, PRF$ ) and the calibration constant  $C_I$ ;

$$\sigma^0 = P_I \frac{H_s^3 V_t}{\sqrt{H_s \cdot PRF \cdot C_I}} \quad (17)$$

Surface reflectivity is then computed inverting Equation (14), using the local surface fractal parameters and slope:

$$R_s^2 = \frac{\chi(H, T, \theta)}{\sigma^0} \quad (18)$$

Finally, surface permittivity is obtained inverting Equation (12), using the values of local slope:

$$\epsilon_s = \left[ \frac{1 - R_s}{1 + R_s} \right]^2 \cos^2 \theta + \sin^2 \theta \quad (19)$$

234

## 235 6. Results

236 Once the effect of surface roughness has been estimated and compensated for, the reflectivity can be  
 237 calibrated according to the assumption that the reference area consists of pure water ice, and the dielectric  
 238 permittivity of the surface can then be estimated from reflectivity through Equation 12. As already discussed  
 239 by Grima et al. (2012), the resulting values are an average of the dielectric permittivity over a thickness of a  
 240 few to several meters from the surface. Estimates of the dielectric properties of the Martian surface from  
 241 SHARAD echoes were produced also by Grima et al. (2012) and by Campbell et al. (2013), using different  
 242 approaches.

243 Grima et al. (2012) modelled the expected properties of the echo in terms of coherent and diffuse  
 244 components, the former dominating when the surface RMS height is small compared to the wavelength,  
 245 while the latter describes scattering from a rougher surface. Exploiting the statistical properties of both

246 strength and phase of the echoes, they determined the dielectric permittivity of a limited number of areas in  
247 which the coherent component of scattering dominated, all located polewards of 70° latitude. Also in this  
248 case, it was necessary to assume that an area in the polar terrains consisted of water ice as a way to provide  
249 an absolute calibration for echo strengths. It was found that the model of the effects of surface scattering fits  
250 the data very well, but such fit becomes less reliable as roughness increases.

251 Campbell et al. (2013) used a simple parameter extracted from surface echoes (the ratio between peak power  
252 and integrated power, called the roughness parameter) to estimate the effect of roughness on surface  
253 scattering at SHARAD wavelengths. This parameter was then computed as a function of RMS slope for  
254 several theoretical models of surface scattering, finding that it is only weakly dependent on the choice of the  
255 scattering law. Thanks to this property, the roughness parameter could be mapped over Mars and used to  
256 identify areas with similar scattering properties. Comparing peak echo strength for such areas, it was inferred  
257 that differences in such strength would be caused only by different dielectric properties. This inference was  
258 not used to quantitatively estimate the surface dielectric permittivity, but rather to compare areas in terms of  
259 higher or lower permittivity, interpreting such difference in terms of higher or lower density of the surface  
260 material.

261 In the present work, it is assumed that the Martian topography behaves as a self-affine fractals so that  
262 scattering can be modelled through a law based on such assumption. Unfortunately, the resolution of existing  
263 global topographic datasets is insufficient to verify if this assumption holds down to scales relevant to  
264 SHARAD scattering (a few meters). To attempt a qualitative validation, we have made use of RMS height  
265 estimates based on the widening of the MOLA pulse echo, presented in Neumann et al. (2003). The area  
266 affecting the MOLA echo is the altimeter footprint, estimated to be approximately 300 m across, while the  
267 RMS height used to evaluate the effect of roughness on scattering has been computed over a moving window  
268 50 km across. As expected, the two datasets provide very different values for RMS height, because  
269 topography is a non-stationary random variable. If the assumption of self-affinity is correct, however, then  
270 RMS height would scale with the size of the area over which it is computed according to the power law  
271 reported as Equation (6) in Orosei et al. (2003):

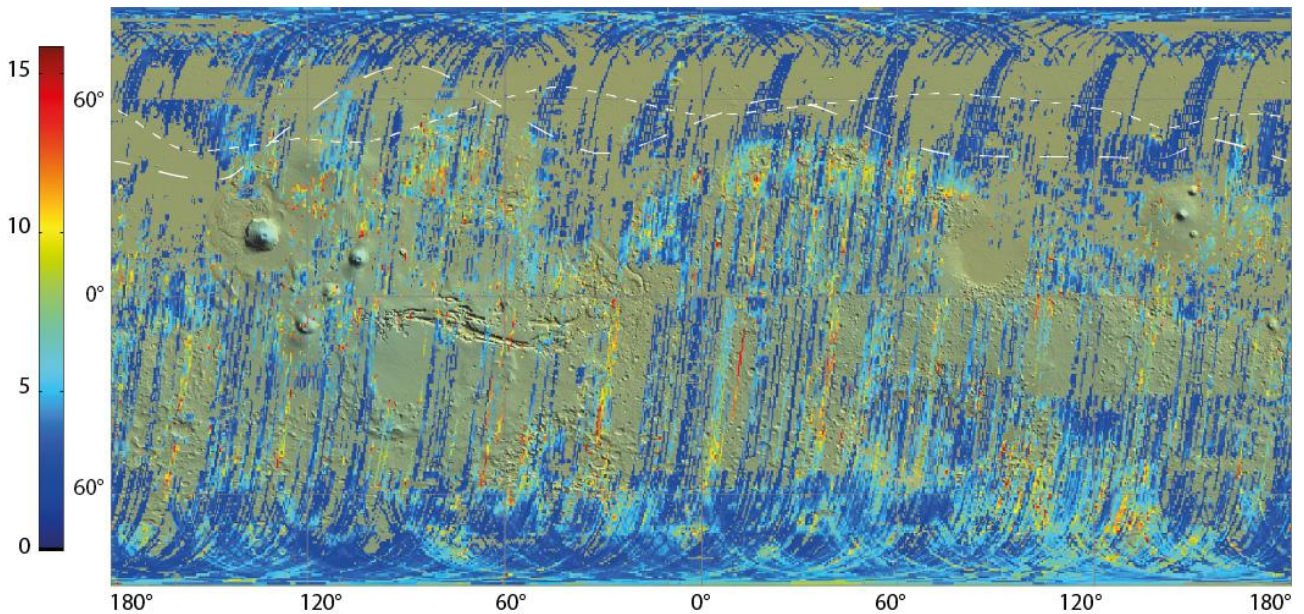
$$272 \quad s_{(L)} = s_0 \left(\frac{L}{L_0}\right)^H \quad (20)$$

273 where  $L$  is the size of the area over which RMS height  $s$  is to be computed,  $s_0$  is the RMS height computed

274 for the area of size  $L_0$ , and  $H$  is the Hurst exponent. We applied Equation (20) to the RMS height computed  
275 from MOLA gridded data to scale it down to the size of the MOLA footprint, and compared it to the RMS  
276 height provided by Neumann et al. (2003). Whenever the two quantities are within the same order of  
277 magnitude, we conclude that the assumption of self-affine topography is valid and consider the  
278 corresponding estimates of the dielectric permittivity as reliable, while we discard estimates obtained in areas  
279 where Equation (20) provides inconsistent values.

280 The final result is presented in Figures 3 and 4. Figure 3 maps the validated estimates of the relative  
281 dielectric permittivity over the Martian surface, whereas Figure 4 reports the absolute error on such estimates  
282 based on the dispersion of estimates within the same map resolution cell. The relative dielectric permittivity  
283 is superimposed to the geological map of Mars by Tanaka et al. (2014) in Supplementary Figure 1. For  
284 interpretation, the dielectric permittivity of non-porous  $\text{CO}_2$  ice is 2.1, that of non-porous water ice is 3.1,  
285 while that of igneous rocks, such as those found on the Martian surface, ranges between 4 and 10, depending  
286 both on composition and porosity (Rust et al., 1999).

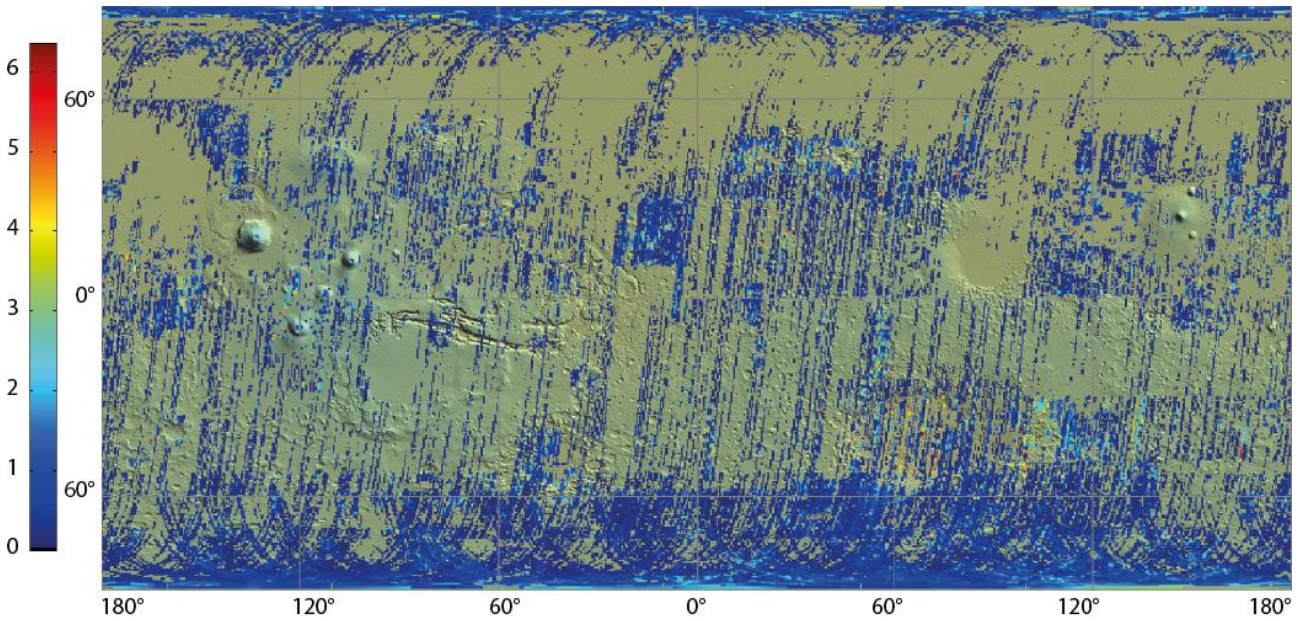
287



288

289 **Figure 3. SHARAD global permittivity constant map of Mars after RMS height correction. The line**  
290 **with long dashes indicates the MARSIS dielectric boundary (6-7) between the highlands and lowlands**  
291 **(after Mouginot et al., 2010). The line with short dashes indicates the boundary between mid-latitude**  
292 **areas in the northern hemisphere having equivalent hydrogen abundance < 8% (south) and > 8%**  
293 **(north) after GRS (after Feldman et al., 2004). Note that the geometry of these boundaries is almost a**  
294 **latitudinal band but does not match the geometry of the dichotomy boundary as define from**

295 topography, suggesting that climate is the main control (Mouginot et al., 2010). The base map on this  
296 figure and the following figures is NASA/JPL/GSFC/MOLA topography.  
297



298  
299 **Figure 4. Permittivity constant standard deviation (std) after RMS height correction**

300

## 301 **7. Discussion**

### 302 **7.1. Global comparison with MARSIS**

303 Comparison between the SHARAD-derived real permittivity constant with the global similar map obtained  
304 from the MARSIS data (Mouginot et al., 2012) reveals the difference between the mean dielectric property  
305 of the subsurface over a thickness of a hundreds of kilometres to kilometres, the penetration depth of  
306 MARSIS, and 15 m at most, the penetration depth of SHARAD. The MARSIS results showed that the  
307 tropics have nearly systematically a high (6-10) permittivity constant (including in some of the lowlands),  
308 whereas higher latitudes and the equator region have significantly lower (2-5). Mouginot et al. (2012)  
309 suggested that evolution from tropical to higher latitudes reflects a difference in water ice content in the  
310 regolith predicted by models of climate interaction with the subsurface. In the northern tropics, SHARAD  
311 also shows a tendency to high dielectric constant, but follows the highlands side of the dichotomy boundary  
312 more accurately. The permittivity constant in the southern tropics, however, is not significantly different  
313 from the equatorial or higher latitude areas, with local exceptions. Implications may be that the ground ice of  
314 the southern hemisphere may be more concentrated close to the surface (meters or tens of meters) than at  
315 depth (hundreds of meters); i.e., the permafrost may have a higher ice content close to the surface than at

316 depth. As porosity lowers the permittivity constant of rocks, an alternative interpretation is that porosity  
317 close to the surface is higher than at depth, and contributes to lower the permittivity constant in the near  
318 subsurface. This explanation makes sense in that increasing lithostatic pressure tends to gradually close pores  
319 at depth. Nevertheless, the good correlation (Mouginot et al., 2012) between the MARSIS-derived  
320 permittivity constant and the Gamma Ray Spectrometer (GRS) results (Boynton et al., 2002; Mitrofanov et  
321 al., 2002) favours the first interpretation. Ground ice stability models all predict that the top of ground ice-  
322 table is in the range of centimetres to several meters (e.g., Mellon and Jakosky, 1993; Mellon et al., 2004),  
323 most frequently in the lower part of the range (Mellon et al., 2004). The next sections present geological  
324 interpretation of the SHARAD-derived real permittivity constant in selected areas.

## 325 **7.2. Hemispheric dichotomy**

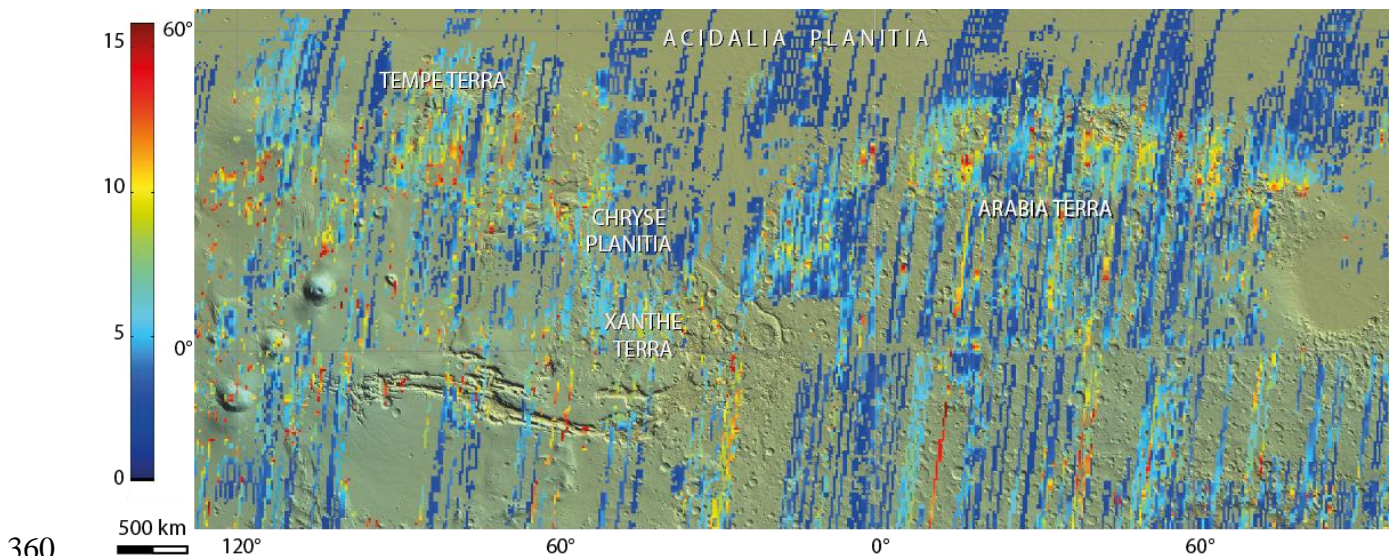
326 The hemispheric dichotomy boundary is in several areas well imaged by SHARAD. It is especially well  
327 delineated in the Vastitas Borealis/Arabia Terra and the Xanthe-Tempe Terrae/Acidalia-Chryse planitiae  
328 transition zones (Figure 5). Narrow highland promontories such as Phlegra Montes and highland portions of  
329 complex highland-lowland transition are also well depicted (see Section 6.3, Figure 7). The dichotomy  
330 boundary is considered to be not only a topographic feature, but also a major crustal transition between the  
331 highlands and the lowlands (e.g., Neumann et al., 2004). In the highlands next to the boundary, two types of  
332 shallow geological discontinuities are inferred from other datasets. On the one hand, orbital imagery shows  
333 that the uppermost part of the highlands crust next to the boundary is layered at the scale of tens of metres  
334 (e.g., Tanaka et al., 2014). On the other hand, another type of layering is inferred from GRS, which indicates  
335 a subsurface having consistently low ice content (2-5% H<sub>2</sub>O) starting at a depth < 1 m (Boynton et al., 2002;  
336 Mitrofanov et al., 2002; Feldman et al., 2004). In the lowlands, there is little evidence of layering from  
337 geomorphology due to the scarcity of subsurface exposures. The GRS water equivalent hydrogen abundance  
338 map (Feldman et al., 2004) does not show any evolution in ice content between the Xanthe-Tempe terrae and  
339 the lowlands next to them on the other side of the dichotomy boundary at a depth < 1 m. In contrary,  
340 SHARAD shows a high (> 10 and up to 15) permittivity constant over a band several hundreds of kilometers  
341 wide in the highlands, and much lower (2-5) in the northern lowlands. Ground ice is therefore expected to be  
342 rare in the highlands in order not to significantly influence the high values of permittivity constant of hard  
343 rock (e.g., Campbell and Ulrichs, 1969). Assuming that low permittivity constant is more due to ice than to

344 rock porosity, an increasing ground ice proportion from the highlands to the lowlands is expected at a depth  
345 greater than what GRS can see, ~1 m (Boynton et al., 2002).

346 The penetration depth of SHARAD below the surface can be retrieved from the equation of an  
347 electromagnetic wave propagating as a function of medium permittivity (Daniels, 1996) as follows:

$$348 \quad d = \frac{c_0 f_c}{2\sqrt{\varepsilon}} \quad (21)$$

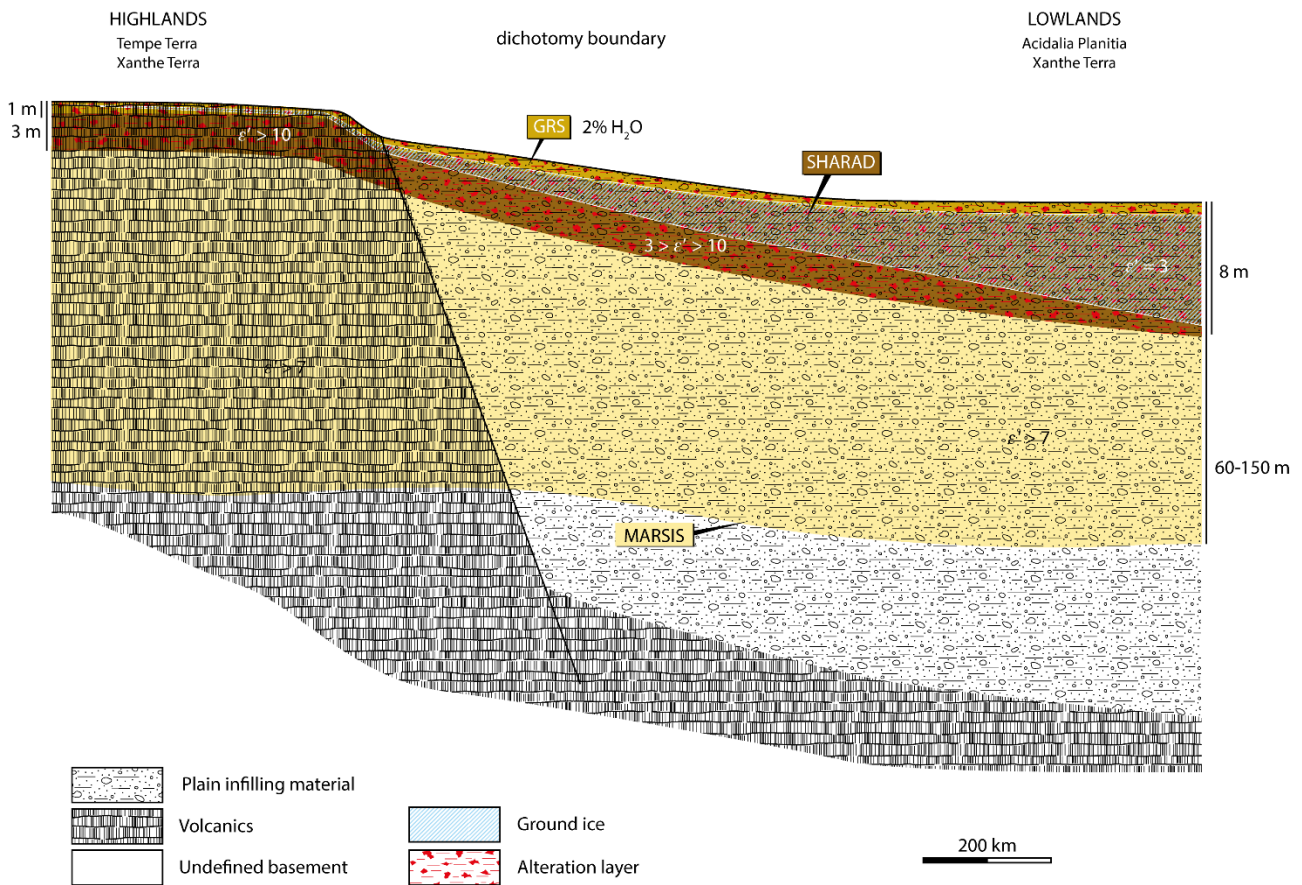
349 where  $d$  is the penetration depth in the first medium,  $c_0$  the speed of light,  $f_c$  the sampling frequency,  $\varepsilon$  the  
350 permittivity of this medium. The penetration depth of SHARAD informs on the depth of the first dielectric  
351 interface encountered from the surface. The highland – lowland transition shows a smooth evolution of this  
352 depth, from < 4 m in the highlands at the onset of the dichotomy boundary in Arabia Terra, Xanthe Terra,  
353 and Tempe Terra, to 8 m and more down in the lowlands. It is unlikely that this interface corresponds to the  
354 highland rock layering because layer thickness, although not formally determined for the lack of appropriate  
355 topography, is expected from geomorphology to be tens of meters, and favour instead the interpretation that  
356 the SHARAD maps may provide a view of the depth of a soil (regolith) containing the permafrost (Figure 6),  
357 or a permafrost layer which has properties, such as ice abundance, substantially different from the underlying  
358 permafrost zone. Since the MARSIS data indicate a high (~7 or more) permittivity constant in the lowlands  
359 of Chryse and Acidalia planitiae, this putative deep permafrost level would be poorly developed.



361 **Figure 5. SHARAD permittivity constant in the dichotomy boundary area between Tempe Terra and**  
362 **Arabia Terra. The dichotomy boundary is underlined by a moderately high (~6) permittivity constant**  
363 **strip bordering the highlands (Tempe Terra, Xanthe Terra, Arabia Terra) and lowlands (Chryse**  
364 **Planitia, Acidalia Planitia), of higher and lower permittivity constant, respectively. The geographic**  
365 **scale is for equatorial regions.**

366

367 A major difference between the SHARAD permittivity constant map (Figure 3) on one side, and the GRS  
368 H<sub>2</sub>O abundance (Feldman et al., 2004) and the MARSIS permittivity constant (Mouginot et al., 2010) maps  
369 on the other side, is that SHARAD locates well the dichotomy boundary south of Chryse, Acidalia, and  
370 Utopia planitiae. In these lowlands, GRS and MARSIS show subsurface properties similar to the properties  
371 of the neighbouring highlands: GRS shows similarly low H<sub>2</sub>O abundance at very shallow depth in the  
372 Martian soil; and MARSIS shows that the subsurface is dominantly dry at the scale of the first hundreds  
373 meters below the surface. According to GRS and MARSIS, this situation changes only starting from 45°-  
374 60°N poleward, where H<sub>2</sub>O abundance increases from 6% to much more toward the pole, and the dielectric  
375 constant gradually decreases to a minimum of 2-3 in the polar region. This pattern agrees well with the  
376 presence of the latitude-dependent, ice-rich mantle conceptualised by Head et al. (2003). The SHARAD map  
377 suggests that the properties of such an ice-rich layer may not depend on latitude only, even though latitude  
378 (hence climate) may be the dominant controlling factor.



379

380 **Figure 6. Cross section of the dichotomy boundary based on the dielectric properties of the subsurface**  
381 **from SHARAD (this work), MARSIS (Mouginot et al., 2010), and inversion of hydrogen abundance**  
382 **from GRS (Feldman et al., 2004), and rock types. Layered volcanic basement of Noachian or Noachian**

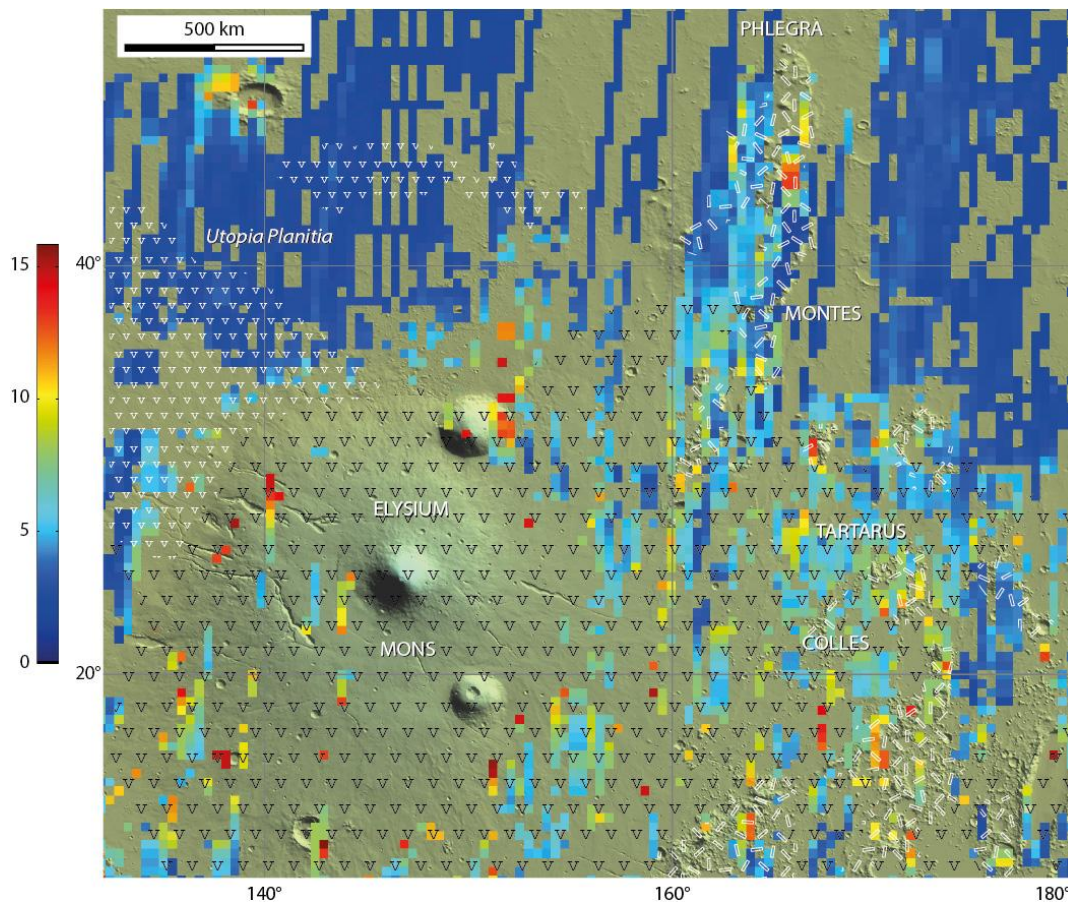
383 **to Hesperian age in the highlands are placed in contact with northern plain infilling material via a**  
384 **hypothetical normal fault system, which is the solution adopted by the authors to explain the**  
385 **dichotomy scarp observed in the topography of this area.**

386

387 Ground ice stability models indicate ground ice instability under the current climate conditions in Chryse,  
388 Acidalia, and Utopia planitiae (e.g., Mellon et al., 2004). There is however ample geomorphological  
389 evidence of surface and ground ice in many latitudes in which ice is not expected. This ice is thought to be  
390 fossil and decaying, inherited from periods of higher planetary obliquity, which has dramatically fluctuated  
391 over the last million years with a ~100 m.y. cyclicity, and probably during the whole history of Mars as well  
392 (Laskar et al., 2004). The ice detected by SHARAD in these lowlands may therefore still be present in the  
393 Martian subsurface in these lowlands due to this climatic inheritance.

### 394 **7.3. Volcanic units: Elysium Mons**

395 SHARAD data processing does not give exploitable results on the major shield volcanoes. Nevertheless,  
396 there are examples where lava flows having different dielectric properties can be separated (Figure 7). At  
397 Elysium, late Amazonian (Tanaka et al., 2014) rugged and hilly volcanic lava field of Tartarus Colles east of  
398 Elysium Mons, probably corresponding to flows from the edifice, have a moderately high average  
399 permittivity constant (5-8) that contrasts with the low permittivity constant of the lowlands of Utopia Planitia  
400 (3-4). In contrast, there is no appreciable difference between the permittivity constant of Utopia Planitia and  
401 a field of long and narrow lava flows of undifferentiated Amazonian age emitted at the northwestern flank of  
402 the edifice. As the SHARAD data were processed in such a way that the effect of surface roughness has been  
403 removed, the observed difference between the dielectric properties of the two lava fields is interpreted not to  
404 be a roughness artefact. It may be due to a differences in the lava alteration profile thickness (for instance  
405 due to hydrothermal water circulation in the flows), or to a younger age of the eastern lava field. Porosity  
406 probably does not play a significant role in minoring the permittivity constant here because pore volume  
407 scales with flow viscosity, and would be expected to be larger for the long narrow, hence fluid northwestern  
408 lava field than for the Tartarus Colles rugged lava field, at the opposite of observations.



409

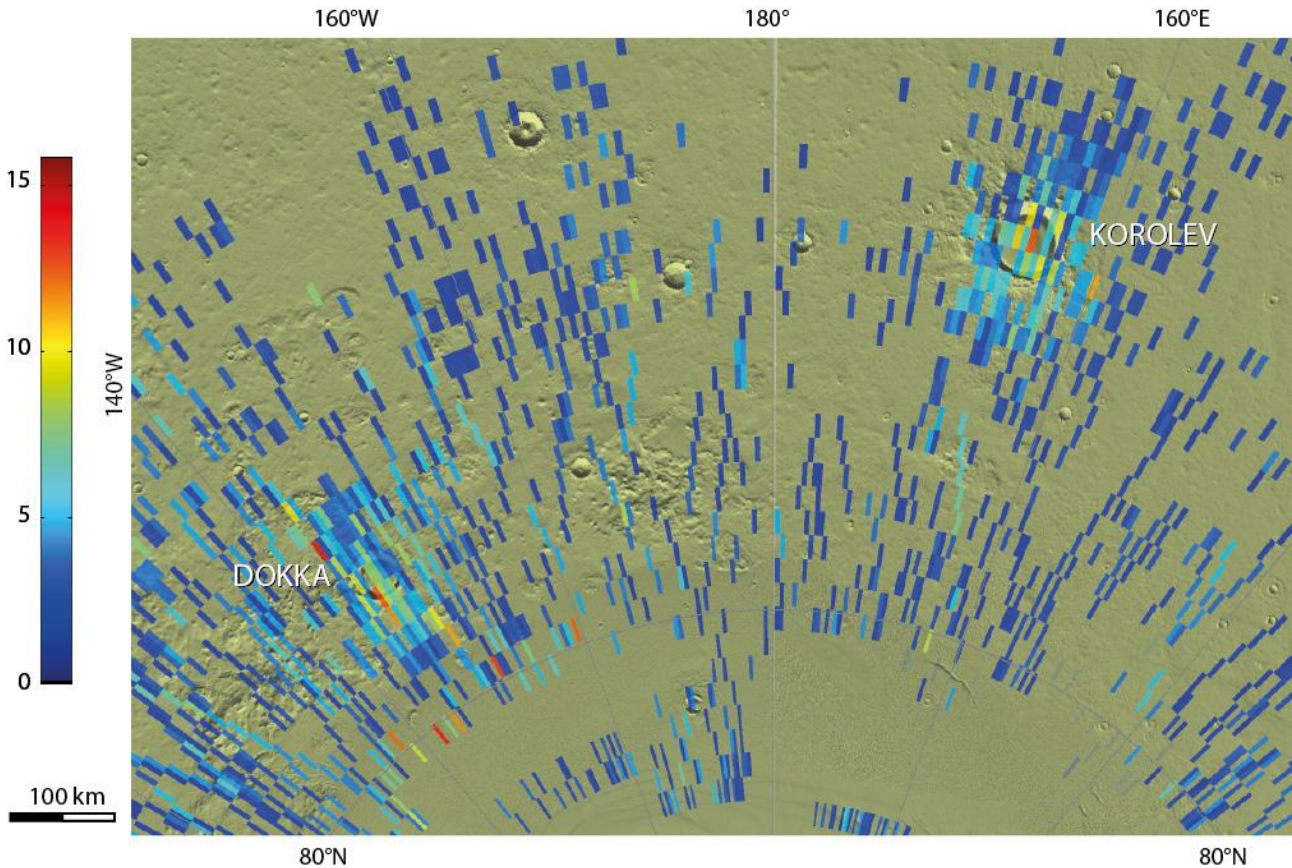
410 **Figure 7. Permittivity constant in the Elysium Mons area. The Phlegra Montes, a Noachian-Hesperian**  
 411 **highland unit (Tanaka et al., 2014), as well the same unit elsewhere (white rectangles) have a higher**  
 412 **permittivity constant than the surrounding lowlands (Utopia Planitia). The permittivity constant of the**  
 413 **Elysium Mons edifice lava flows, of late Hesperian age, and the eastern, rugged, hilly flows of Tartarus**  
 414 **Colles, ascribed to the late Amazonian (both with a black "V" pattern) is usually above 7, and the first**  
 415 **permittivity discontinuity is < 4 m. The western Elysium flows, ascribed to Amazonian (white "v"**  
 416 **patterns), which form long, fluid flows, have the same low permittivity constant as the lowlands (3-4)**  
 417 **and the first discontinuity is deeper (above 6 m). The geographic scale is for the southern part of the**  
 418 **map.**

419

#### 420 **7.4. Ice-filled craters in the northern lowlands**

421 Two of the largest impact craters in the North Polar region, Korolev and Dokka, have distinct dielectric  
 422 properties compared to the surrounding lowlands. The permittivity constant of the lowlands is < 4 whereas  
 423 Korolev and Dokka is higher, locally as high as 11-12 (Figure 8). CTX and HiRISE images show that both  
 424 craters are filled with decimeter- to meter-thick layered material (Conway et al., 2012), the stratigraphy of  
 425 which is underlined by variations in rock fragment or dust contents. This infilling is mapped as equivalent to  
 426 the polar cap layered deposits (Tanaka et al., 2014). TES, THEMIS, and CRISM data have shown that the

427 infilling of Korolev is composed of water-ice or a dominantly water-ice regolith (Armstrong et al., 2005;  
428 Conway et al., 2012). Thermophysical mapping by Jones et al. (2014) suggests that this material is  
429 dominated by ice-cemented soil and exposed ice. SHARAD radargrams have shown that the thickness of the  
430 infilling approaches 2 km and confirm in cross section the geomorphological observations that the layers are  
431 similar to those observed in the north polar layered deposits (e.g., Brothers and Holt, 2013).



432  
433 **Figure 8. The permittivity constant of the ice-filled Korolev (a) and Dokka (b) craters is higher than**  
434 **the permafrost-rich surrounding lowlands. The map is computed with a SHARAD pixel size of 0.1°.**  
435 **Korolev is located at 72.77°N, 164.58°E, and Dokka at 77.17°N, 214.24°E.**

436  
437 The low permittivity constant of the lowlands is consistent with ice-rich permafrost, as indicated by  
438 morphology (e.g., Tanaka et al., 2014). Higher values inside Korolev and Dokka may denote (1) a  
439 dominantly rocky content at surface; (2) the presence of snow. Dry snow usually has permittivity constant  
440 between air, 1, and ice, 3.15, (Evans, 1965; Kovacs et al., 1995), but for wet snow it is between ice, 3.15, and  
441 water, ca. 80. The permittivity constant of snow also critically depends on the shape and orientation of  
442 crystals, some realistic structures resulting in values much higher than ice (Evans, 1965). Daniels (2004, p.  
443 90) reports 6-12 as the permittivity constant of firn; (3) impurities in ice or snow (e.g., Evans, 1965). Such

444 impurities could be fine windblown rock particles such as, for instance, from basalt (of permittivity constant  
445 between 7 and 10; Campbell and Ulrich, 1969), or sulfates (6.5; Martinez and Byrnes, 2001) that would have  
446 formed from basalt alteration (Niles and Michalski, 2009); (4) retreat of out-of-equilibrium ice, producing  
447 water vapor on the surface and at subsurface, hence the permittivity constant measured by SHARAD, before  
448 it escapes in the atmosphere (Schorghofer and Forget, 2012); (5) although measurements and experiments on  
449 sea ice have usually been conducted at a radar frequency in the microwave range, they suggest that in the  
450 SHARAD frequency range too, brine included in ice would help increase the permittivity constant to the  
451 measured values, depending on ice temperature, brine volume fraction, shape ratio and distribution of brine  
452 inclusions in ice (Vant et al., 1978; Stogryn and Desargant, 1985; Pringle et al., 2009).

453 High-resolution imagery argues against the first hypothesis. In both craters, the ice layers are observed to  
454 have flown from the crater walls, i.e., from the lowland permafrost. In Korolev crater, the ice layers are  
455 partly and unconformably covered by lighter-toned deposits (Supplementary Figure 2, a) that remind of  
456 snow megadunes, dunes and ripples on terrestrial glaciers (e.g., Arcone et al., 2012). The blue channel on  
457 HRSC colour imagery of Korolev crater is more strongly reflective when the ice layers are not covered by  
458 snow dunes (Supplementary Figure 3), supporting analogy with snow dunes on top of blue ice in terrestrial  
459 polar regions such as e.g. the Mina Bluff area, Antarctica (Supplementary Figure 2, c). Similar to terrestrial  
460 instances, blue ice could form in these craters by sublimation (e.g., Bintaja, 1999), and snow dunes would  
461 form either by snow precipitation, transport, and accumulation at lower elevations in the crater. In Dokka  
462 crater, the lighter-toned dunes are seen to develop on the slope of ice layer cliffs, suggesting that gravity is  
463 involved in their formation (Supplementary Figure 2, b). These observations favour interpretation of high  
464 dielectric constant in these craters by the presence of snow (2) and ice retreat (4), but ice impurities are  
465 clearly visible in the ice layers and their contribution (3) cannot be discarded. The permittivity constant of  
466 dry rocks does not exceed 10, however (Campbell and Ulrich, 1969; Martinez and Byrnes, 2001; Daniels,  
467 2004), suggesting that rocky particles mixed with ice or snow would probably not explain, alone, the  
468 permittivity constant up to 12 locally observed in Korolev and Dokka. Wet rock has a permittivity constant  
469 that easily exceeds 10, but is not stable at the surface of Mars currently and therefore discarded.

470 Accumulation of brine ice (5) cannot be ruled out without information on the composition and abundance of  
471 dissolved elements. These brines would need to significantly differ from brines identified on Mars so far,  
472 which give birth to dark flows for which there is no evidence in Korolev and Dokka craters.

473

## 474 **8. Conclusion**

475 This study presents a model of inverse scattering to extract the real part of the derived real permittivity of  
476 Mars using SHARAD level 1b data and the MOLA topographic dataset. Results obtained by inverting the  
477 SHARAD data are showed in a surface permittivity map. Permittivity was obtained by correcting the effect  
478 of noise and rugosity using the geometry provided by MOLA and the SHARAD auxiliary data of level 1b.  
479 To this end, the Hurst and topothesy coefficients were evaluated over the whole Martian surface.

480 Correlation with surface geology was sought. The permittivity map follows the variations of the dichotomy  
481 boundary more accurately than the GRS hydrogen abundance map and the MARSIS dielectric map do,  
482 indicating that in the SHARAD penetration depth range, the ice-rich layer is not latitude-dependent only.  
483 Although SHARAD does frequently not give exploitable results on the major shield volcanoes, in some  
484 instances lava flows can be distinguished, perhaps due to different thickness or alteration. The permittivity  
485 constant of Korolev and Dokka, the two large ice-filled impact craters near the North Polar Cap, is  
486 significantly higher than the permafrost-rich surrounding lowlands, a feature which is not well understood  
487 but could be related to the existence of snow dunes in these craters.

488 An improvement of the current analysis would be the use of higher resolution topographic data, either to  
489 derive more accurate values of statistical parameters controlling scattering at the scales of SHARAD  
490 wavelengths, or to directly simulate the effect of surface scattering on the radar echo and compare it to the  
491 real echo, as in Mouginot et al. (2010, 2012). The increasing availability of such high-resolution topography  
492 - at least locally - and greater computing power make this last option increasingly more viable.

493

## 494 **Acknowledgements**

495 This work was supported by the TEAM programme of the Foundation for Polish Science (project  
496 TEAM/2011-7/9), co-financed by the European Union within the framework of the European Regional  
497 Development Fund.

498

## 499 **References**

500 Alberti, G., Castaldo, L., Orosei, R., Frigeri, A., Cirillo, G., 2012. Permittivity estimation over Mars by using  
501 SHARAD data: the Cerberus Palus area. *J. Geophys. Res.* 117, E09008, doi:10.1029/2012JE004047.

502 Arcone, S.A., Jacobel, R., Hamilton, G., 2012. Unconformable stratigraphy in East Antarctica: Part 1. Large  
503 firn coseqs, recrystallized growth, and model evidence for intensified acculation. *J. Glaciol.* 58, 240-264,  
504 doi:10.3189/2012JoJ11J044.

505 Armstrong, J.C., Titus, T.N., Kieffer, H.H., 2005. Evidence for subsurface water ice in Korolev crater, Mars.  
506 *Icarus* 174, 360-372.

507 Bintaja, R., 1999. On the glaciological, meteorological, and climatological significance of Antarctic blue ice  
508 areas. *Rev. Geophys.* 37, 337-359.

509 Bogorodsky, V., Bentley, C., Gudmandsen, P., 1985. *Radioglaciology*. Reidel, Dordrecht.

510 Boynton, W.V., Feldman, W.C., Squyres, S.W., Prettyman, T.H., Brückner, J., Evans, L.G., Reedy, R.C.,  
511 Starr, R., Arnold, J.R., Drake, D.M., Englert, P.A.J., Metzger, A.E., Mitrofanov, I., Trombka, J.I., d'Uston,  
512 C., Wänke, H., Gasnault, O., Hamara, D.K., Janes, D.M., Marcialis, R.L., Maurice, S., Mikheeva, I., Taylor,  
513 G.J., Tokar, R., Shinohara, C. 2002. Distribution of hydrogen in the near surface of Mars: evidence for  
514 subsurface ice deposits. *Science* 297, 81-85.

515 Brothers, T.C., Holt, J.W., 2013. Korolev, Mars: growth of a 2-km thick ice-rich dome independent of, but  
516 possibly linked to, the north polar layered deposits. 44<sup>th</sup> Lunar Planet. Sci. Conf., Houston, abstract 3022.

517 Campbell, B.A., Putzig, N.E., Carter, L.M., Morgan, G.A., Phillips, R.J., Plaut, J.J., 2013. Roughness and  
518 near-surface density of Mars from SHARAD radar echoes. *J. Geophys. Res.* 118, 436-450.

519 Campbell, M.J., Ulrichs, J., 1969. Electrical properties of rocks and their significance for lunar radar  
520 observations. *J. Geophys. Res.* 74, 5867-5881.

521 Conway, S. J., Hovius, N., Barnie, T., Besserer, J., Le Mouélic, S., Orosei, R., Read, N.A., 2012. Climate-  
522 driven deposition of water ice and the formation of mounds in craters in Mars' north polar region. *Icarus* 220,  
523 174-193.

524 Currie, N. C., 1984. *Techniques of Radar Reflectivity Measurement*. Norwood, MA Artech House.

525 Daniels, D. J., 1996. Surface-penetrating radar. *Electronics and Communication Engineering Journal* 8, 165-  
526 182, doi: 10.1049/ecej:19960402.

527 Daniels, D.J. (Ed.), 2004. *Ground penetrating radar – 2nd Ed.*, Inst. Electrical Eng., London, 734 p.

528 Evans, S., 1965. Dielectric properties of ice and snow – a review. *J. Glaciol.* 5, 773-792.

529 Feldman, W.C., Prettyman, T.H., Maurice, S., Plaut, J.J., Bish, D.L., Vaniman, D.T., Mellon, M.T., Metzger,  
530 A.E., Squyres, S.W., Karunatillake, S., Boynton, W.V., Elphic, R.C., Funsten, H.O., Lawrence, D.J., Tokar,

531 R.L., 2004. Global distribution of near-surface hydroge on Mars. *J. Geophys. Res.* 109, E09006,  
532 doi:10.1029/2003JE002160.

533 Franceschetti, G., Iodice, A., Migliaccio, M., Riccio, D., 1999. Scattering from natural rough surfaces  
534 modeled by fractional brownian motion two-dimensional processes, *IEEE Trans. Antennas Propagation* 47,  
535 1405-1415.

536 Franceschetti, G., Riccio, D., 2007. *Scattering, natural surfaces, and fractals*. Elsevier Academic Press,  
537 Burlington, San-Diego, London.

538 Grima, C., Kofman, W., Mouginot, J., Phillips, R. J., Hérique, A., Biccari, D., Seu, R., Cutigni, M., 2009.  
539 North polar deposits of Mars: Extreme purity of the water ice. *Geophys. Res. Lett.* 36, L03203,  
540 doi:10.1029/2008GL036326.

541 Grima, C., Kofman, W., Herique, A., Orosei, R., Seu, R., 2012. Quantitative analysis of Mars surface radar  
542 reflectivity at 20 MHz. *Icarus* 220, 84-99.

543 Head, J.W., Mustard, J.F., Kreslavsky, M.A., Mililliken, R.E., Marchant, D.R., 2003. Recent ice ages on  
544 Mars. *Nature* 426, 797-802.

545 Ivanov, A., Safaeinili, A., Plaut, J., Milkovich, S., Picardi, G., 2006. Observations of the layering structure in  
546 the Martian Polar Layered Deposits with the MARSIS instrument, AGU Fall Meeting, San Francisco,  
547 abstract P13D-07.

548 Jones, E., Caprarelli, G., Mills, F.P., Doran, B., Clarke, J., 2014. An alternative approach to mapping  
549 thermophysical units from Martian thermal inertia and albedo data using combination of unsupervised  
550 classification techniques. *Remote Sens.* 6, 5184-5237, doi:10.3390/rs6065184.

551 Kovacs, A., Gow, A.J., Morey, R.M., 1995. The in-situ dielectric constant of polar firm revisited. *Cold*  
552 *regions Sci. Technol.* 23, 245-256.

553 Kreslavsky, M.A, Head, J.W, 1999. Kilometer-scale slopes on Mars and their correlation with geologic units:  
554 initial results from Mars Orbiter Laser Altimeter (MOLA) data. *J. Geophys. Res.* 104, 21911-21924.

555 Laskar, J., Correia, A.C.M., Gastineau, M., Joutel, F., Levrard, B., Robutel, P., 2004. Long term evolution  
556 and chaotic diffusion of insolation quantities of Mars. *Icarus* 170, 343-364.

557 Mandelbrot, B.B., 1983. *The Fractal Geometry of Nature*. W.H. Freeman and co., San Francisco.

558 Martinez, A., Byrnes, A.P., 2001. Modeling dielectric-constant values of geologic materials: an aid to  
559 ground-penetrating radar data collection and interpretation. *Current Res. Earth Sciences, Bull 247*, part 1, 16  
560 p.

561 Mellon, M.T., Jakosky, B.M., 1993. Geographic variations in the thermal and diffusive stability of groundice  
562 on Mars. *J. Geophys. Res.* 98, 3345-3364.

563 Mellon, M.T., Feldman, W.C., Prettyman, T.H., 2004. The presence and stability of ground ice in the  
564 southern hemisphere of Mars. *Icarus* 169, 324-340.

565 Mitrofanov, L., Anfimov, D., Kozyrev, A., Litvak, M., Sanin, A., Tretyakov, V., Krylov, A., Shvetsov, V.,  
566 Boynton, W., Shinohara, C., Hamara, D., Saunders, R.S., 2002. Maps of subsurface hydrogen from the high  
567 energy neutron detector, Mars Odyssey. *Science* 297, 78-81.

568 Mouginit, J., Pommerol, A., Beck, P., Kofman, W., Clifford, S.M., 2012. Dielectric map of the Martian  
569 northern hemisphere and the nature of plain filling materials. *Geophys. Res. Lett.* 39, L02202,  
570 doi:10.1029/2011GL050286.

571 Mouginit, J., Pommerol, A., Kofman, W., Beck, P., Schmitt, B., Hérique, A., Grima, C., Safaeinili, A., 2010.  
572 The 3-5 MHz global reflectivity map of Mars by MARSIS/Mars Express: implications for the current  
573 inventory of subsurface H<sub>2</sub>O. *Icarus* 210, 612-625, doi: 10.1016/j.icarus.2010.07.003.

574 Neumann, G. A., Abshire, J. B., Aharonson, O., Garvin, J. B., Sun, X., Zuber, M. T., 2003. Mars Orbiter  
575 Laser Altimeter pulse width measurements and footprint-scale roughness. *Geophys. Res. Lett.* 30, 1561.

576 Neumann, G.A., Zuber, M.T., Wicczorek, M.A., McGovern, P.J., Lemoine, F.G., Smith, D.E., 2004. *J.*  
577 *Geophys. Res.* 109, E08002, doi:10.1029/2004JE002262.

578 Niles, P.B, Michalski, J., 2009. Meridiani Planum sediments on Mars formed through weathering in massive  
579 ice deposits. *Nature Geosci.* 2, 215-220, doi:10.1038/NGEO438.

580 Ono, T., Kumamoto, A., Nakagawa, H., Yamaguchi, Y., Oshigami, S., Yamaji, A., Kobayashi, T., Kasahara,  
581 Y., Oya, H. 2009. Lunar Radar Sounder Observations of Subsurface Layers Under the Nearside Maria of the  
582 Moon. *Science* 323, 909-912, doi: 10.1126/science.1165988.

583 Orosei, R., Bianchi, R., Coradini, A., Espinasse, S., Federico, C., Ferriccioni, A., Gavrishin, A.I., 2003. Self-  
584 affine behavior of Martian topography at kilometer scale from Mars Orbiter Laser Altimeter data, *J.*  
585 *Geophys. Res.* 108 (E4), 8023, doi:10.1029/2002JE001883.

586 Phillips, R.J., and 14 co-authors, 1973. Apollo Lunar Sounder Experiment. *NASA Spec. Pub.* 330 (22), 1-26.

587 Picardi, G., and 12 co-authors, 2004. MARSIS: Mars Advanced Radar for Subsurface and Ionosphere  
588 Sounding, Mars Express: the scientific payload. ESA Publications Division, 51-69.

589 Pringle, D., Dubuis, G., Eicken, H., 2009. Impedance measurements of the complex dielectric permittivity of  
590 sea ice at 50 MHz: pore microstructure and potential for salinity monitoring. *J. Glaciol.* 55, 81-94.

591 Rust, A. C., Russell, J. K., Knight, R. J., 1999. Dielectric constant as a predictor of porosity in dry volcanic  
592 rocks. *J. Volcanol. Geotherm. Res.* 91, 79-96.

593 Seu, R., Phillips, R.J., Biccari, D., Orosei, R., Masdea, A., Picardi, G., Safaeinili, A., Campbell, B.A., Plaut,  
594 J.J., Marinangeli, L., Smrekar, S.E., Nunes, D.C., 2007. SHARAD sounding radar on the Mars  
595 Reconnaissance Orbiter, *J. Geophys. Res.* 112, E05S05, doi:10.1029/2006JE002745.

596 Schorghofer, N., Forget, F., 2012. History and anatomy of subsurface ice on Mars. *Icarus* 220, 1112-1120.

597 Slavney S., Orosei R., 2008. SHALLOW RADAR REDUCED DATA RECORD SOFTWARE  
598 INTERFACE SPECIFICATION, retrieved from PDS Geosciences Node: [http://pds-  
599 geosciences.wustl.edu/missions/mro/sharad.htm](http://pds-geosciences.wustl.edu/missions/mro/sharad.htm)

600 Smith, D.E., and 23 co-authors, 2001. Mars Orbiter Laser Altimeter (MOLA): Experiment Summary after  
601 the First Year of Global Mapping of Mars, *J. Geophys. Res.* 106, 23689-23722, doi: 10.1029/2000JE001364.

602 Stogryn, A., Desargant, G.J., 1985. The dielectric properties of brine in sea ice at microwave frequencies.  
603 *IEEE Trans. Antennas Propagation AP-33*, 523-532.

604 Tanaka, K.L., Skinner, J.A., Dohm, J.M., Irwin, R.P., III, Kolb, E.J., Fortezzo, C.M., Platz, T., Michael,  
605 G.G., Hare, T.M., 2014. Geologic map of Mars. U.S. Geol. Surv. Sci. Invest. Map 3292, scale 1:20,000,000,  
606 pamphlet 43 p., doi:10.3133/sim3292.

607 Ulaby, F.T., Moore, R.K., Fung, A.K., 1986. *Microwave Remote Sensing: Active and Passive*, vol. III,  
608 *Volume Scattering and Emission Theory, Advanced Systems and Applications*. Artech House, Inc., Dedham,  
609 Massachusetts.

610 Vant, M.R., Ramseier, R.O., Makios, V., 1978. The complex-dielectric constant of sea ice at frequencies in  
611 the range 0.1-40 GHz. *J. Appl. Phys.* 49, 1254-1280.

612

613 **Figure captions**

614 Figure 1. Observation 0659501 001 SS19 700A is an example of a SHARAD radargram showing reflections  
615 due to dielectric interfaces at the surface and in the subsurface from which is extracted the surface power echo in

616 linear scale by the automatic routine and low-pass filtered and weighted with linear least squares with a  
617 second degree polynomial model.

618 Figure 2. Mars topography evaluated using MOLA topographic data

619 Figure 3. SHARAD global permittivity constant map of Mars after RMS height correction. The line with  
620 long dashes indicates the MARSIS dielectric boundary (6-7) between the highlands and lowlands (after  
621 Mouginot et al., 2010). The line with short dashes indicates the boundary between mid-latitude areas in the  
622 northern hemisphere having equivalent hydrogen abundance  $< 8\%$  (south) and  $> 8\%$  (north) after GRS (after  
623 Feldman et al., 2004). Note that the geometry of these boundaries is almost a latitudinal band but does not  
624 match the geometry of the dichotomy boundary as defined from topography, suggesting that climate is the  
625 main control (Mouginot et al., 2010). The base map on this figure and the following figures is  
626 NASA/JPL/GSFC/MOLA topography.

627 Figure 4. Permittivity constant standard deviation (std) after RMS height correction

628 Figure 5. SHARAD permittivity constant in the dichotomy boundary area between Tempe Terra and Arabia  
629 Terra. The dichotomy boundary is underlined by a moderately high ( $\sim 6$ ) permittivity constant strip bordering  
630 the highlands (Tempe Terra, Xanthe Terra, Arabia Terra) and lowlands (Chryse Planitia, Acidalia Planitia),  
631 of higher and lower permittivity constant, respectively. The geographic scale is for equatorial regions.

632 Figure 6. Cross section of the dichotomy boundary based on the dielectric properties of the subsurface from  
633 SHARAD (this work), MARSIS (Mouginot et al., 2010), and inversion of hydrogen abundance from GRS  
634 (Feldman et al., 2004), and rock types. Layered volcanic basement of Noachian or Noachian to Hesperian  
635 age in the highlands are placed in contact with northern plain infilling material via a hypothetical normal  
636 fault system, which is the solution adopted by the authors to explain the dichotomy scarp observed in the  
637 topography of this area.

638 Figure 7. Permittivity constant in the Elysium Mons area. The Phlegra Montes, a Noachian-Hesperian  
639 highland unit (Tanaka et al., 2014), as well the same unit elsewhere (white rectangles) have a higher  
640 permittivity constant than the surrounding lowlands (Utopia Planitia). The permittivity constant of the  
641 Elysium Mons edifice lava flows, of late Hesperian age, and the eastern, rugged, hilly flows of Tartarus  
642 Colles, ascribed to the late Amazonian (both with a black "V" pattern) is usually above 7, and the first  
643 permittivity discontinuity is  $< 4$  m. The western Elysium flows, ascribed to Amazonian (white "v" patterns),

644 which form long, fluid flows, have the same low permittivity constant as the lowlands (3-4) and the first  
645 discontinuity is deeper (above 6 m). The geographic scale is for the southern part of the map.

646 Figure 8. The permittivity constant of the ice-filled Korolev (a) and Dokka (b) craters is higher than the  
647 permafrost-rich surrounding lowlands. The map is computed with a SHARAD pixel size of  $0.1^\circ$ . Korolev is  
648 located at  $72.77^\circ\text{N}$ ,  $164.58^\circ\text{E}$ , and Dokka at  $77.17^\circ\text{N}$ ,  $214.24^\circ\text{E}$ .

649

## 650 **Supplementary material**

651 Supplementary Figure 1. Dielectric constant map of Mars with the geologic map of Tanaka et al. (2014) as a  
652 background.

653 Supplementary Figure 2. High-resolution views of part of Korolev (a) and Dokka (b) crater infillings,  
654 showing the possible presence of snow, from comparison with snow on terrestrial glaciers; for comparison,  
655 ice and snow landforms in Antarctica: (c) glacial lobe down the Haselton Icefall (Calkin, 1971) of the  
656 Victoria Land dry valleys, and (d) snow dunes on blue ice surface, a consequence from snow precipitation,  
657 transport by winds, and accumulation at the surface of blue ice next to Minna Bluff, McMurdo ice shelf.  
658 Colour views of Korolev and Dokka craters: HRSC images H5726\_0001 and H5488\_0000, respectively;  
659 channels IR/GR/BL (ESA/DLR/FU Berlin). Grey level views of Korolev and Dokka craters: CTX image  
660 mosaics (Korolev: west: G22\_026936\_2528\_XI\_72N197W, east: B02\_010387\_2529\_XN\_72N195W;  
661 Dokka: B02\_010385\_2572\_XN\_77N146W). Haselton Icefall: image ©2015 Digital Globe in Google Maps.  
662 Field view of snow ripples on the Ross ice shelf next to Minna Bluff on blue ice. Field view retrieved on  
663 February 14, 2016 from *Glaciers online*:

664 [http://www.swisseduc.ch/glaciers/antarctic/mcmurdo\\_ice\\_shelf/ice\\_shelf\\_surface/index-en.html](http://www.swisseduc.ch/glaciers/antarctic/mcmurdo_ice_shelf/ice_shelf_surface/index-en.html).

665 Supplementary Figure 3. Spectral cross-sections of Korolev crater infilling using the near-infrared, green,  
666 and blue bands (red, green, and blue tones, respectively) of HRSC image H5726\_0001. The surfaces covered  
667 by ice uncovered by snow dunes (mainly along profile #1, on the left side of profiles #2 to #5 and on the  
668 right side of profile #6) are significantly bluer than surfaces covered by ice and snow.

Figure 1  
[Click here to download high resolution image](#)

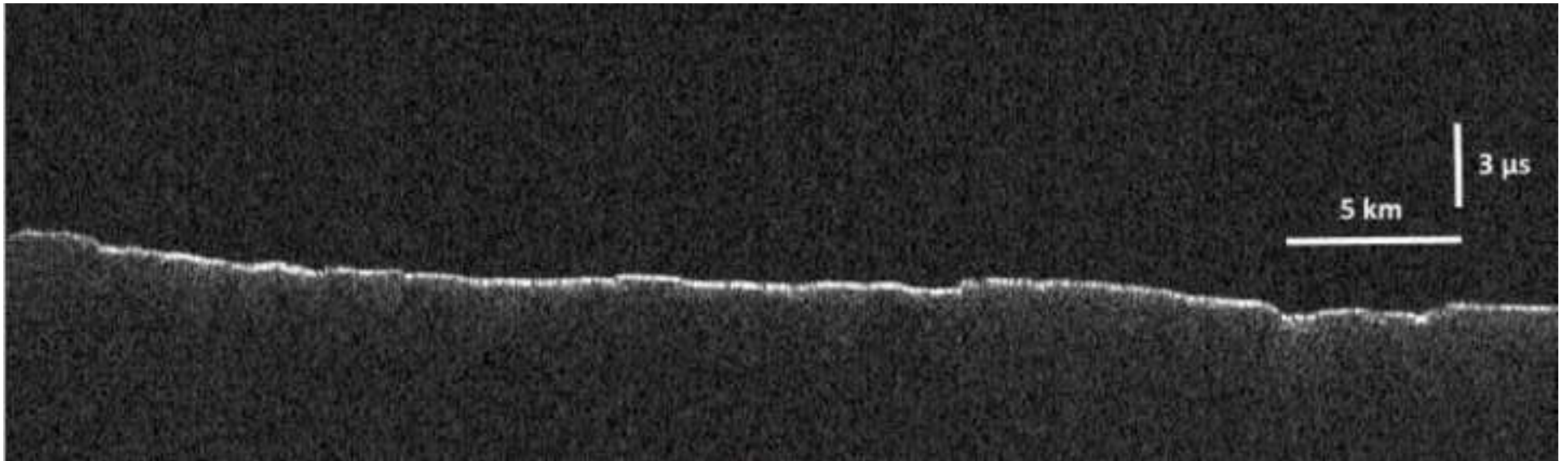


Figure 2  
[Click here to download high resolution image](#)

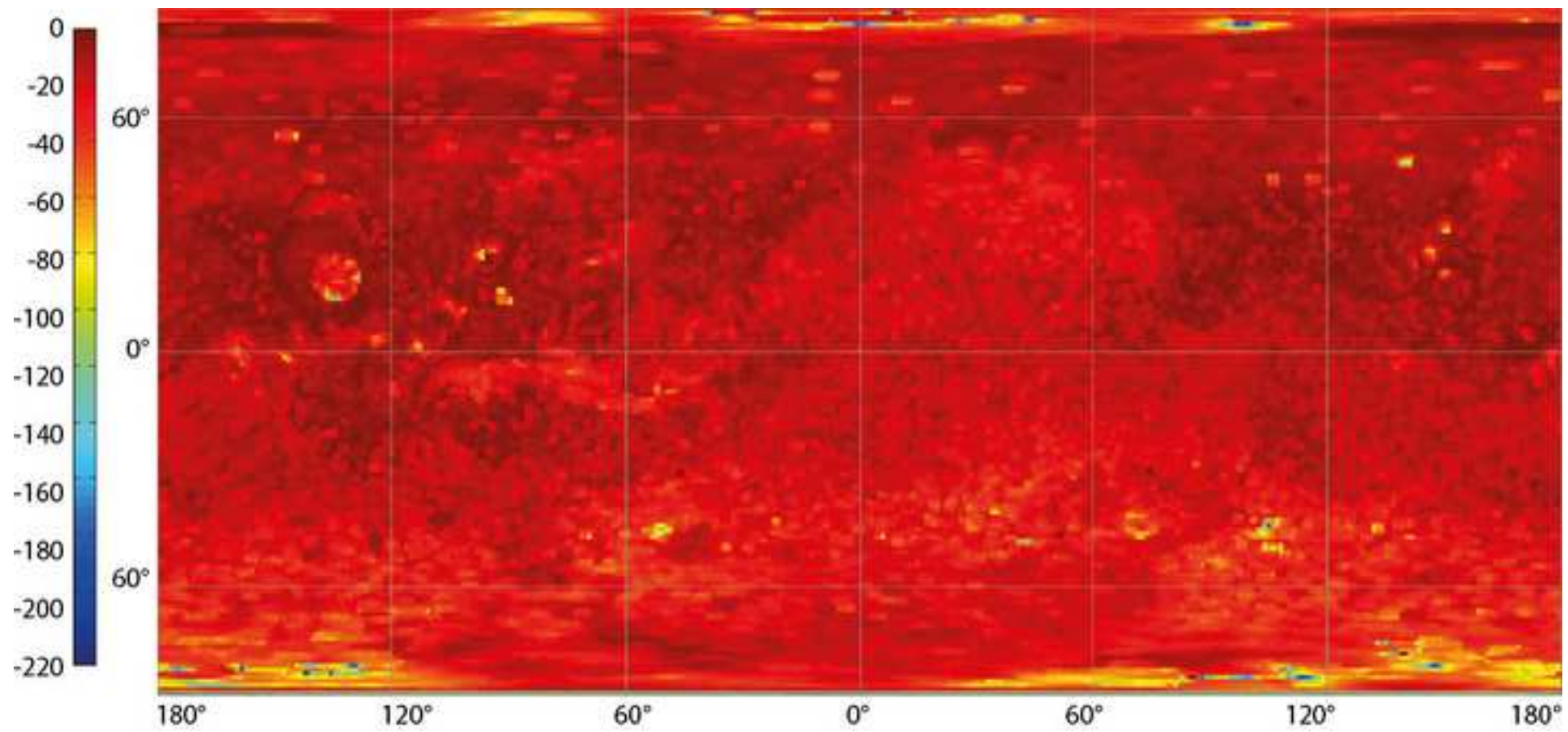


Figure 3  
[Click here to download high resolution image](#)

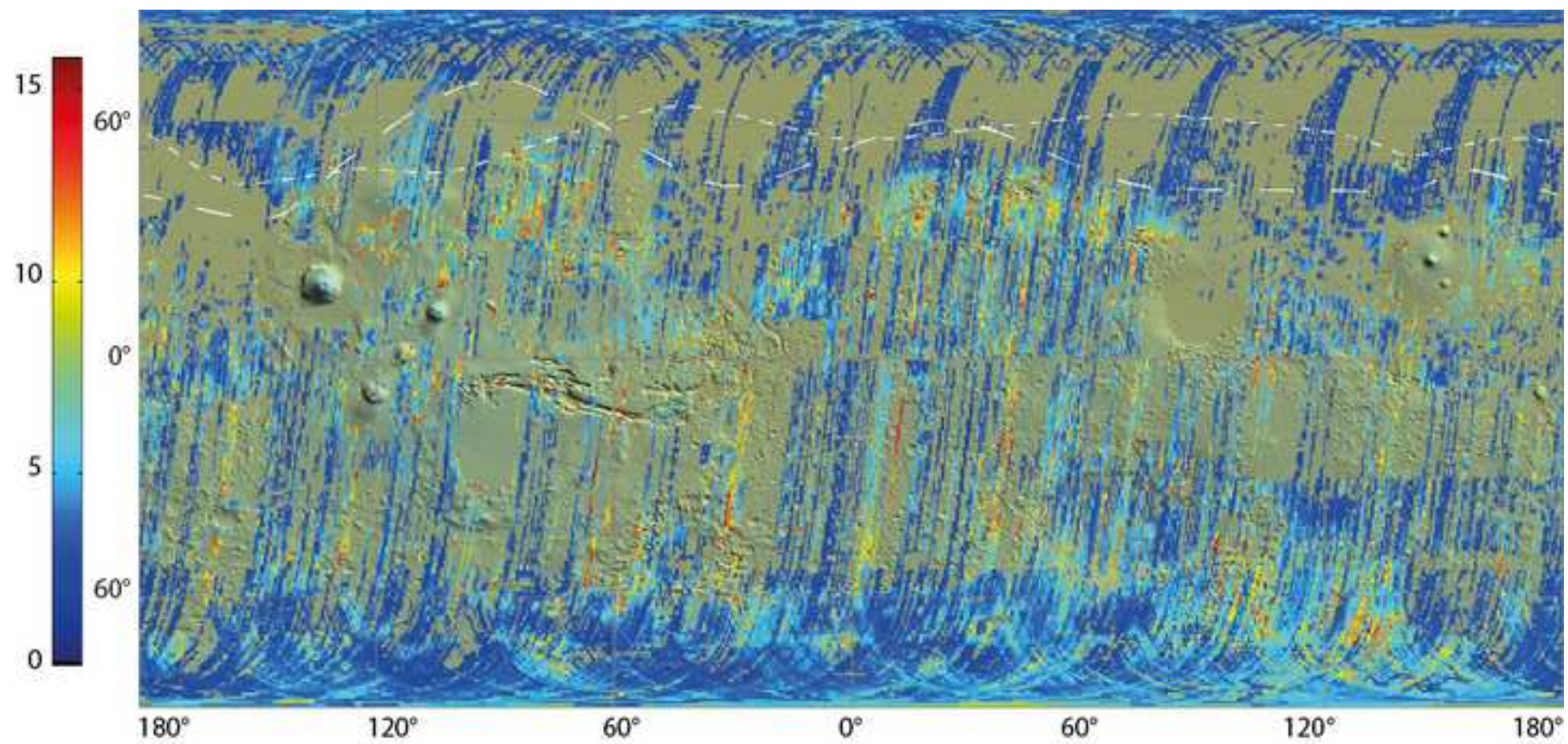




Figure 5  
[Click here to download high resolution image](#)

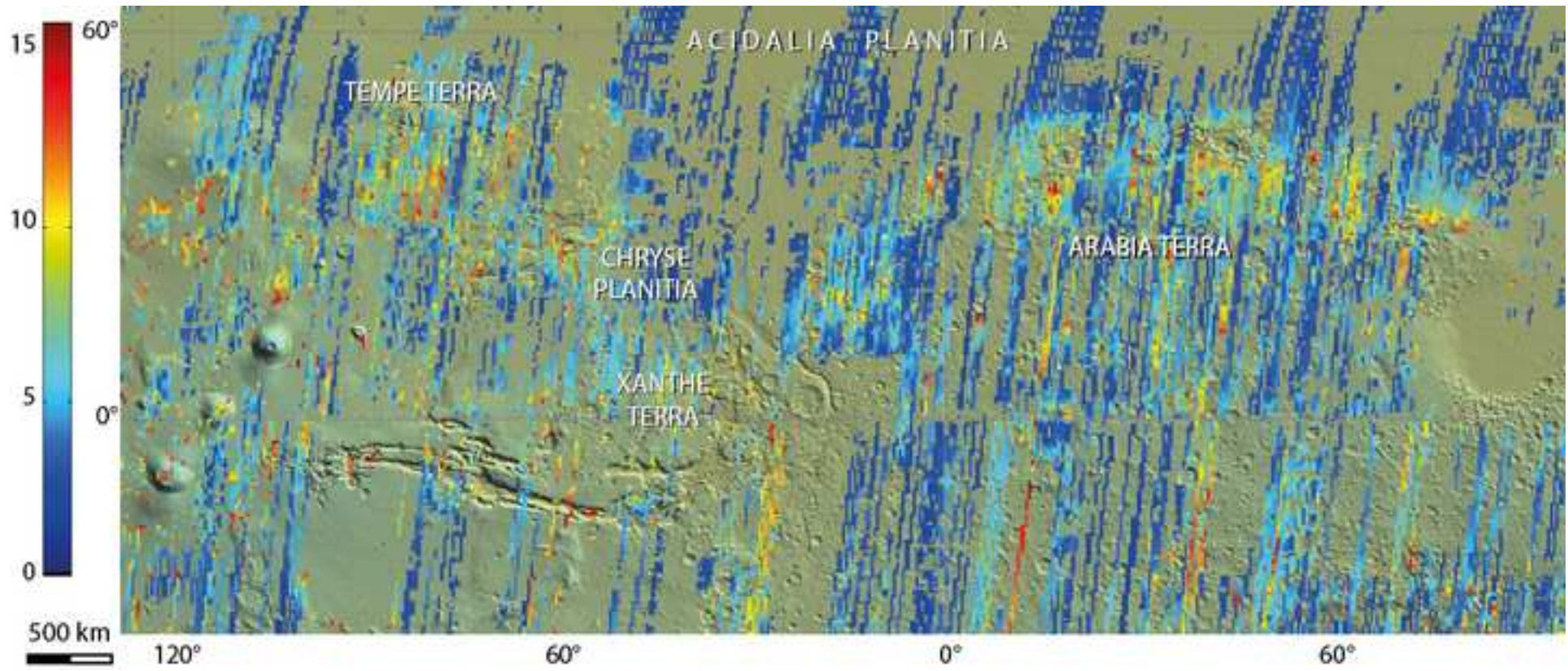


Figure 6  
[Click here to download high resolution image](#)

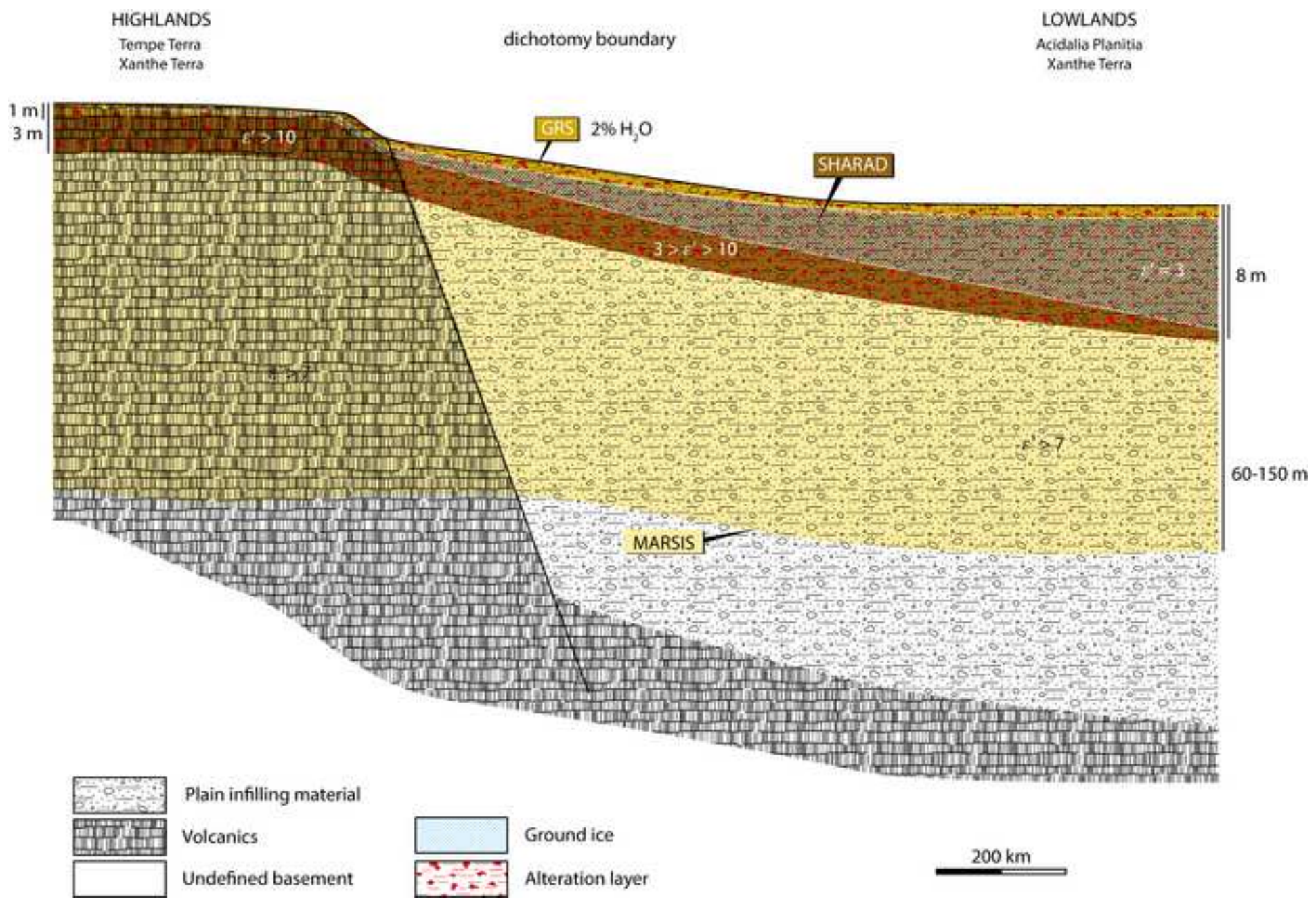


Figure 7  
[Click here to download high resolution image](#)

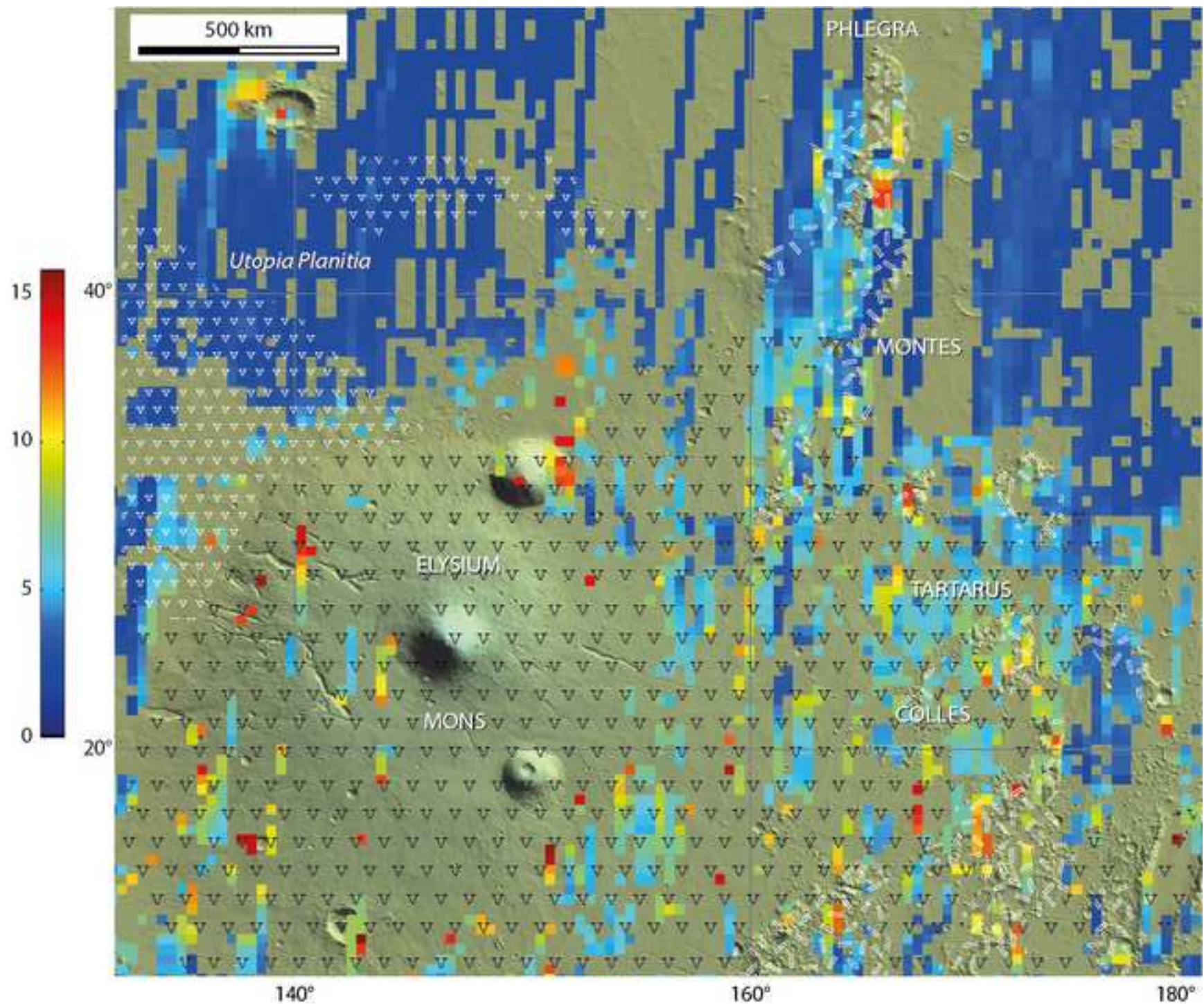
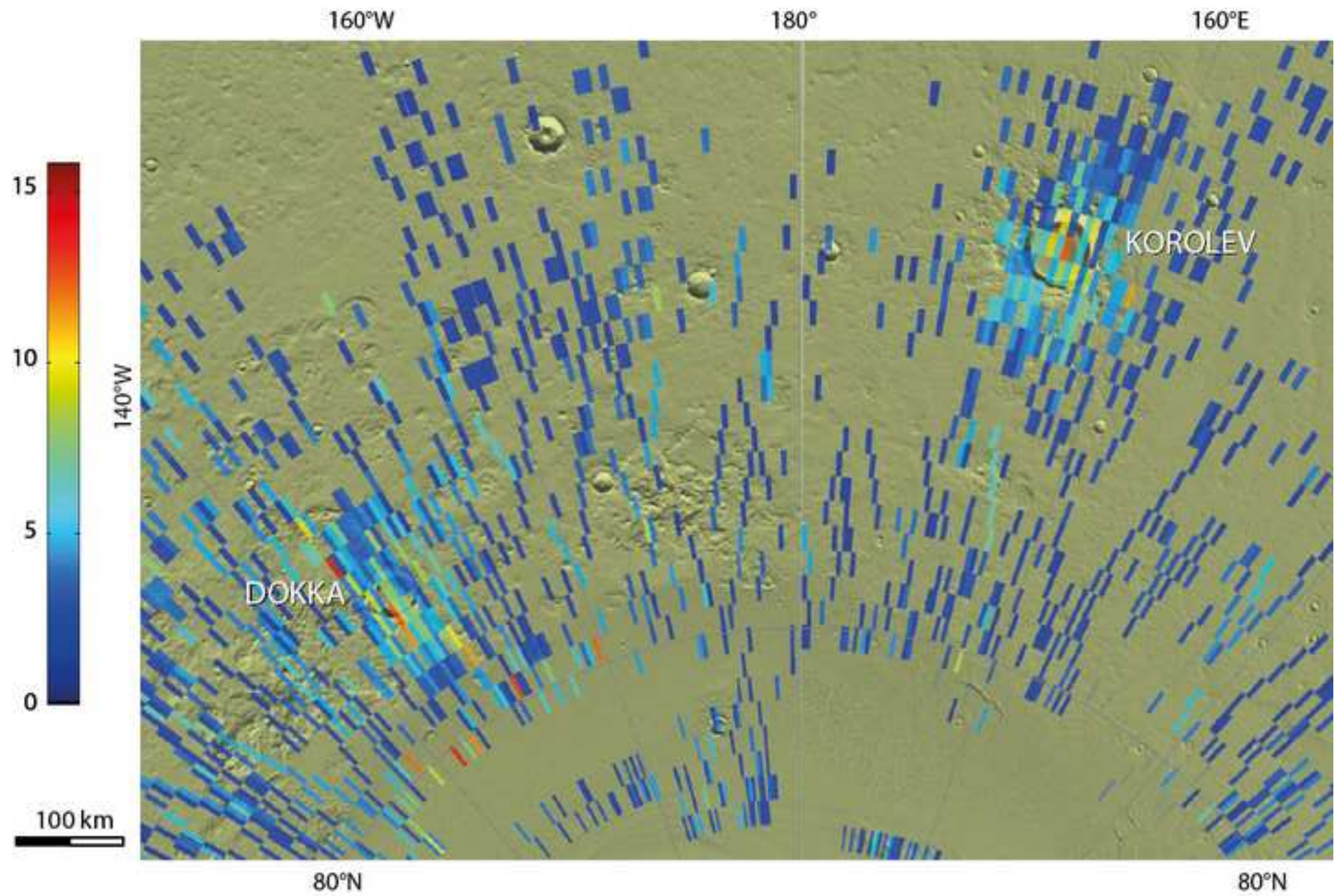


Figure 8  
[Click here to download high resolution image](#)



**Supplementary Figure 1**

[Click here to download Supplementary material for online publication only: Supplementary Figure 1\\_SHARAD diel constant on g](#)

**Supplementary Figure 2**

[Click here to download Supplementary material for online publication only: Supplementary Figure 2\\_Antarctica glacier comparis](#)

**Supplementary Figure 3**

[Click here to download Supplementary material for online publication only: Supplementary Figure 3\\_Korolev HRSC IR\\_GR\\_BL t](#)